ABSTRACT

BOLES, JOHN A. Hybrid LES/RANS Simulation of a 10° Double-Fin Crossing Shock Flow at Mach 8.28. (Under the direction of Professor Jack R. Edwards).

The simulation of a Mach 8.28 10-degree double-fin crossing shock flow using a hybrid large-eddy / Reynolds-averaged Navier-Stokes (LES/RANS) solver is presented in this work. The solver blends a Menter two-equation model for RANS with a Yoshizawa one-equation subgrid model for the LES calculations. The solver uses a flow-dependent transition function based on wall distance and a modeled form of the Taylor microscale. Turbulent boundary layers are initiated and sustained in the inflow region using a recycling/rescaling technique applied to the fluctuation fields. The hybrid LES/RANS model is tested using both Menter's Baseline (BSL) and Shear Stress Transport (SST) models for the RANS closure. These results are compared to pure Menter BSL and SST RANS results as well as with the experimental data of Kussoy and Horstman [1]. This study concludes that while the hybrid LES/RANS model outperforms RANS calculations in the inflow region where the flow is nominally two-dimensional, it significantly overpredicts the wall heat transfer rates in the region of the crossing shock interaction. Possible explanations for this behavior as well as plans for future attempts at solutions to these shortcomings are provided.

Hybrid LES/RANS Simulation of a 10° Double-Fin Crossing Shock Flow at Mach 8.28

by

John A. Boles

A thesis submitted to the Graduate Faculty of
North Carolina State University
in partial fulfillment of the
requirements for the Degree of
Master of Science

Aerospace Engineering

Raleigh, NC

2007

Approved By:

Dr. D. Scott McRae	Dr. Richard D. Gould

Dr. Jack R. Edwards
Chair of Advisory Committee

Biography

John Boles was born on July 1, 1982 to Phillip and Lee Ann Boles in High Point, North Carolina. From the age of 3 until his move to North Carolina State University at 18, he lived in nearby Greensboro. Here, he discovered a love for science, math and the arts (particularly music). His third grade teacher, Mr. Moore first sparked his interest in space and the challenges of manned spaceflight with his inspired teaching. Mr. Ritchie instilled a sense of excitement and confidence about math in his fifth grade classroom.

John attended Aycock Middle School and graduated from Page High School in 2000. In his high school years he had the honor of attending Governor's School for Instrumental Music playing the cello. He also received his Eagle Scout Award as a member of Troop 109.

He decided to attend North Carolina State University for aerospace engineering. An undergraduate introduction to CFD course taught by his current adviser, Dr. Edwards, first piqued his interest in the world of computational fluid modeling. John graduated in 2004 with a BS in aerospace engineering. He then immediately started graduate research under the supervision of Dr. Edwards.

When not in the lab, John enjoys listening to and playing all kinds of music. He also enjoys film (particularly documentaries, independent cinema and foreign cinema) as well as camping and racquetball.

Acknowledgements

I would like to thank Dr. Edwards for his endless patience, support and for first introducing me to computational fluid dynamics; his clear presentation of the material in classes is a testament to his expertise in the field. I would also like to thank Dr. McRae and Dr. Gould for serving on my thesis committee. Dr. Hassan and all the people in the hypersonics lab provided valuable guidance and advice. Patrick Keistler and Adam Amar deserve special recognition for their camaraderie through countless classes over the years and for their friendship.

My family and friends deserve unending thanks for their love and support. They have been incredibly patient with my seemingly ever-changing plans for my education. Erin Gillespie has been a partner and a friend for the past year. I thank her for her patience with my many late nights in the lab and plans that changed frequently when homework and projects were more time-consuming than I had anticipated.

I also must thank the NC State University High Performance Computing for providing computing resources and support. I would also like to thank Taitech Inc. for their funding support (contract T002-34-01) under subcontract from Air Force Research Laboratory (F33615-02-C-2234) and the Army Research Office for funding my current work (contract W911NF-06-1-0299).

Contents

List of Figures

List of Tables

Nomenclature

Roman Letters

A	model constant
$\tilde{A}$ - $\tilde{G}$	flux Jacobians used for planar relaxation in time advancement
C_d	model constant
C_s	model constant
C_{smag}	Smagorinsky constant
C_μ	model constant
C_p	specific heat at constant pressure
C_v	specific heat at constant volume
d	distance to nearest wall
d^+	$= u_\tau d/\nu$, wall coordinate
E	total energy per unit mass
$\vec{E}$	inviscid flux in the x direction
$\vec{\mathcal{E}}$	inviscid flux in the ξ direction
F_1	blending function for Menter's Model
$\vec{f_e}$	external force vector
f	blending function for rescaling procedure

H	total enthalpy
I	rothalpy $= H - \vec{u} \cdot \vec{w}$
`int`	function to take the integer part of a real number
J	Jacobian for coordinate transformation
K	coefficient of thermal conductivity
k	turbulent kinetic energy
M	Mach number
p	pressure
P_k	turbulent kinetic energy production term
q_i	laminar heat flux vector
Q_j	subgrid scale heat flux vector
R	gas constant
R	steady residual
R_β	constant for hybrid LES/RANS blending function
R_δ	constant for hybrid LES/RANS blending function
$\mathcal{R}$	unsteady residual
S	source vector or strain rate
T	temperature
t	time
$\mathcal{T}$	time period
U	conservative variable vector
u,v,w	velocity components
$\mathcal{U}$, $\mathcal{V}$, $\mathcal{W}$	contravariant velocity components

$\vec{u}$	velocity vector
W_f	work of external forces
W	weighting function for inner and outer boundary layer for rescaling procedure
$\vec{x}$	position vector
x, y, z	Cartesian coordinates

Greek Letters

β	model constant for ω equation
β^*	model constant for k equation
Γ	blending function for hybrid LES/RANS model
γ	specific heat ratio and Menter model constant
Δ	filter width
δ	boundary layer thickness
η	model coefficient
κ	$= 0.41$; Kármán's constant
λ	Taylor microscale
μ	molecular viscosity
μ_t	turbulent molecular viscosity
ν	kinematic viscosity coefficient
ξ, η, ζ	curvilinear coordinates
ξ_{x_i}, η_{x_i}, ζ_{x_i}	metric derivatives
ρ	density
σ_ω	model constant for ω equation
σ_k	model constant for k equation

τ_{ij}	stress tensor
τ_{ij}^{R}	Reynolds stress tensor
τ_{ij}^{S}	subgrid scale stress tensor
ϕ	generic model constant for blending function
ω	turbulence frequency

Superscripts

c	convective component
k	time integration subiteration level
n	time level
p	pressure component

Subscripts

1/2	cell interface
i	inviscid
i,j,k	cell indices, spatial coordinates
inl	inlet
inn	inner boundary layer
L,R	left and right states
out	outer boundary layer
rec	recycle
resc	rescaled quantity
t	total
v	viscous

Accents

$\vec{}$	vector
$\bar{}$	time-averaged quantity
$'$	fluctuation
$''$	Favre-averaged
$\tilde{}$	density-averaged

Abbreviations

BSL	Baseline
CFD	Computational Fluid Dynamics
DDES	Delayed Detached Eddy Simulation
DES	Detached Eddy Simulation
DNS	Direct Numerical Simulation
LES	Large Eddy Simulation
LNS	Limited Numerical Scales
MSD	Modeled Stress Depletion
RANS	Reynolds-averaged Navier-Stokes
SGS	subgrid-scale
SST	Shear Stress Modification
TKE	Turbulent kinetic energy

Chapter 1

Introduction

The evolution of turbulence modeling has depended on a balance of numerous factors. The chief concern of a turbulence model is to accurately reflect the physics of a given fluid flow. Another consideration is the simplicity of a model's implementation into a computational fluid dynamics (CFD) code. As would be expected, the more accurate methods typically require more computational storage and are more computationally expensive. Turbulence modeling also requires the resolution of many different spatial and temporal scales in its computations. These requirements bring to bear the factors of computational requirements for both processing power and storage. Different approaches to these problems have yielded a myriad of models for turbulent flow. Many of these models are well-suited to only a small subset of physical problems. Applicability of a model to a specific problem or to a broad set of problems is another consideration that must be taken into account when developing or choosing a turbulence model.

Direct numerical simulation (DNS) can theoretically be used for all imaginable types of problems. DNS is simply a complete time-accurate, three-dimensional solution of the Navier-Stokes equations. In theory, this would be an accurate numerical solution to the exact flow equations. Unfortunately, these computations are generally prohibitively expensive computationally at this time for flows of practical interest. The main limitation is that to use a DNS simulation, vastly different scales must be resolved by the grid. The computational domain must be able to resolve the smallest fluctuations as well as have a domain large enough to contain the largest fluctuations. For the foreseeable future, DNS will likely only be used for very simple canonical cases for use in verifying other methods [2, 3] since its computational costs are so high.

The Large Eddy Simulation (LES) approach was developed to reduce some of the computational requirements of DNS. This method directly calculates the large fluctuations (or "eddies") while using mathematical models to represent the smallest, subgrid-scale (SGS) eddies. The justification for this modification is that the large eddies carry most of the Reynolds stress, while the smaller eddies are weaker, and thus less critical [4]. Because of this modeling of the smallest eddies, the grid resolution requirements for LES are not nearly as strict as those of a DNS simulation. A major limitation of LES modeling is that for wall-bounded flows, the turbulent scales near the wall are all small. Thus the grid resolution required near the wall is nearly equal to that of a DNS simulation.

The Reynolds-averaged Navier-Stokes (RANS) approach is the cheapest computationally of the three major approaches to turbulence modeling. RANS relies on time-averaged versions of the Navier-Stokes equations to predict the turbulent stresses. This method performs quite well for attached flows, especially considering its modest computational requirements. Unfortunately it is not equipped to accurately predict highly-separated or unsteady flows – conditions more suited to an LES or DNS calculation.

Hybrid models attempt to combine the best elements of LES and RANS to make a computationally efficient method relative to full LES computations. Spalart, et al. [5] developed one of the most widely-used methods of this sort, known as Detached Eddy Simulation or DES. The idea behind this approach is to use the wall distance to determine at any given point whether the solver should use RANS or LES, with RANS close to the wall. This approach, in its basic form, relies solely on geometry and the computational mesh to define the distinct RANS and LES regions. As a result, grid generation is very important and is impractical for internal flows, as the flow structure normally cannot be predicted, thus a suitable grid cannot be generated to properly handle the positioning of the RANS/LES juncture. Forsythe et al. [6] have used the DES method to simulate the F-15E at a high angle of attack and at a flight Reynolds number. Reasonable grid convergence was reported by the author. The DES simulation showed similar results to a RANS simulation of the flow, while requiring approximately seven times the computational cost of the RANS method on the same grid. With this additional computational cost, the DES method had the advantage of being able to capture the unsteadiness of the flow – which is of importance to the aeroacoustics and aeroelasticity community, among others. Aside from grid generation, another challenge of DES is the initialization of LES fluctuating quantities at the RANS/LES interface from the Reynolds-averaged flow quantities in the

RANS region [7]. Dahlström, et. al [8, 9, 10] proposed turbulent fluctuations obtained from generic DNS simulations be added to the momentum equation at the LES side of the unsteady-RANS/LES juncture. Basu et. al [7] attempted two different DES variants, the first variant increases the turbulent kinetic energy dissipation rate and the second reduces the turbulent kinetic energy itself. Both variants used a limiter that is a function of the local turbulent length scale and the local grid dimensions to achieve their respective variations.

Spalart et al. [11] devised the Delayed Detached Eddy Simulation (DDES) recently to remedy the problem of "ambiguous" parallel grid densities. This problem relates to the fundamental workings of the DES method. The original DES relied solely on grid spacing to determine RANS and LES zones. Whether due to flow conditions (such as a thick boundary layer or boundary layer separation) or complex geometry, some grids had parallel grid spacing that was small enough in relation to the boundary layer thickness to trigger an LES designation by DES while still in the boundary layer. This switch to LES erroneously reduced the eddy viscosity in the boundary layer region without being able to resolve the required velocity fluctuations for LES content. This in turn reduced the Reynolds stress without the necessary increase in resolved stress. Spalart et al. refer to this phenomenon as Modeled Stress Depletion or MSD. They have proposed a solution to this problem which is inspired by the Shear Stress Transport method of Menter [12]. This modification calls for a redefinition of the DES length scale to depend on an eddy viscosity model as well as the grid spacing, in the hopes of avoiding MSD. It was concluded that this simple modification prevents MSD except in extreme grid cases.

Batten et al. [13] developed what they have termed as the Limited Numerical Scales (or LNS) approach. This method attempts to generalize the embedding of LES (or DNS) regions within a RANS-modeled flow. This is achieved by identifying the resolvable and unresolvable fractions of the turbulence kinetic energy and their dissipation rates using the ratio of the product of the turbulence length and velocity scales for the RANS and LES (or DNS) formulations.

There is particular interest and research in the area of shock-wave/boundary-layer interaction. The prevalence of these interactions in nearly all high-speed flows makes a detailed understanding of the phenomena very desirable. The double-fin crossing shock cases such as those reported by Kussoy and Horstman [1], Thivet et al. [14], Knight et al.[15], Gaitonde et al. [16] and Garrison et al. [17] provide highly three-dimensional, unsteady test cases of oblique shock-wave/boundary layer interactions for turbulent flow models. The

structure of these flows has been investigated for decades. There are predominant features of all the cases involving hypersonic flow over a flat plate with sharp, double-fin geometries. These include oblique shock-waves formed at the leading edges of the fins. These oblique shock-waves cause separation in the turbulent boundary layer downstream and consequent separation shocks. The separation shocks and the incident "inviscid shocks" reflect off of each other. For more detail of the shock structure see Garrison et al. [17]. Vortical structures are formed because of this separation. The main vortical structures of the flow are two counter-rotating helical vortices that are roughly stream-aligned. There are also counter-rotating vortices from entrained flow under the main vortices. These vortices bring high-energy fluid into the interaction [16]. More detail about the vortex structure can be found in [16]. The flow reattaches close to the fin wall along a line of reattachment. The flow structure on the bottom wall was detailed in [15, 16, 17].

There have been numerous attempts to model the double-fin shock-wave/turbulent-boundary-layer interaction computationally. Gaitonde et al. [16] used a Baldwin-Lomax algebraic model in conjunction with the compressible Navier-Stokes equations to model a Mach 8.28 symmetric 15° case. This study showed good agreement with experimental data except for off-center heat transfer rates. Narayanswami et al. [18] performed the same case as Gaitonde et al. using both the Baldwin-Lomax algebraic model and the two-equation Rodi (modified $k-\epsilon$) turbulence model. This study showed similar results to Gaitonde, noting good agreement with experimental data for yaw angle and surface pressure but an overprediction of heat transfer with significant disagreement for off-center data. Thivet et al. [14] performed three double-fin interactions at Mach 4 ($7^\circ \times 7^\circ$, $7^\circ \times 11^\circ$ and $11^\circ \times 11^\circ$). This study focused on improvement in the heat transfer predictions using the k-ω RANS model. It concluded that the high levels of heat transfer could be linked with high levels of TKE and the attachment to the bottom wall of the vortices downstream of the primary oblique shock-wave. Heat transfer coefficients were lowered (though not to experimental levels) by implementing the Durbin correction [19] which introduces a dependence of the model constant C_μ on the velocity gradients.

Some have attempted to improve the traditional RANS-type formulations in order to be able to predict these types of flows more accurately. Gerolymos et. al [20, 21] applied new methods for computing Reynolds stresses that do not depend on geometry or wall distance. Wall distances and unit normals are replaced by functions of the gradients of turbulent length scale and anisotropy tensor invariants (see [21] for a detailed discussion of

model details, development and validation). The authors concluded that not only did this modification allow for implementation of the turbulence model into complex geometries, but also improved the results of their model on simple flows.

Strides have been made at NCSU to develop a hybrid LES/RANS method that relies upon the flow itself, not the grid, to determine a smooth RANS-to-LES transition. In this model the RANS model is taken to be a near-wall closure in an otherwise LES-modeled flow [22]. This approach has shown promising results for nominally two-dimensional shock-boundary layer interactions [23, 24]. This study will attempt to simulate a highly three-dimensional internal flow. The simulation is based on the double-fin 10 degree crossing shock interaction performed by Kussoy and Horstman [1]. This interaction features strong separation due to an interaction between the boundary layer with oblique shock waves. The motivation for using a hybrid model for this flow is the potential to better predict off-center properties of the flow which are difficult with RANS calculations. Also, heat transfer predictions for RANS calculations are not as accurate as required and a time-accurate model with the abilities of LES to capture separated flows could prove valuable in accurately predicting heat transfer. To the knowledge of the author, there have been no numerical simulations of the 10 degree case of Kussoy and Horstman, though there have been many simulations of the stronger 15-degree case [25, 18, 16].

The study details the governing equations involved in deriving this hybrid model, followed by the numerical procedure used to discretize and solve the governing equations. A description of the particular methods for this hybrid model including the recycling/rescaling technique and the blending function are detailed. A comparison of the hybrid LES simulation of this flow with experimental data and RANS solutions follows. Flat plate profile data for the incoming boundary is first used to test the model's ability to capture the correct boundary layer growth. Finally, the full interaction is discussed at length. Conclusions based on these results are then discussed with an outline of future plans for work on the model.

Chapter 2

Governing Equations

2.1 Navier-Stokes Equations

The governing equations for fluid dynamics are the Navier-Stokes equations. These equations consist of equations for energy, momentum and continuity. The Navier-Stokes equations without body forces or external heat addition can be written as follows:

$$\frac{\partial \rho}{\partial t} + \frac{\partial \rho u_i}{\partial x_i} = 0 \tag{2.1}$$

$$\frac{\partial \rho u_i}{\partial t} + \frac{\partial \rho u_i u_j}{\partial x_j} = -\frac{\partial p}{\partial x_i} + \frac{\partial \tau_{ij}}{\partial x_j} \tag{2.2}$$

$$\frac{\partial \rho E}{\partial t} + \frac{\partial \rho H u_i}{\partial x_i} = \frac{\partial}{\partial x_i}\left(u_j \tau_{ij} - q_i\right) \tag{2.3}$$

where

$$E = C_v T + \frac{1}{2}\rho u_i u_i \tag{2.4}$$

$$H = C_p T + \frac{1}{2}\rho u_i u_i \tag{2.5}$$

$$\tau_{ij} = \mu\left(\frac{\partial u_i}{\partial x_j} + \frac{\partial u_j}{\partial x_i} - \frac{2}{3}\frac{\partial x_k}{\partial u_k}\delta_{ij}\right) \tag{2.6}$$

$$q_i = -\frac{\mu C_p}{Pr}\frac{\partial T}{\partial x_i} \tag{2.7}$$

When doing computational fluid dynamics problems, it is often more convenient for these equations to be written in what is known as conservative form:

$$\frac{\partial \vec{U}}{\partial t} + \frac{\partial \vec{E}}{\partial x} + \frac{\partial \vec{F}}{\partial y} + \frac{\partial \vec{G}}{\partial z} = \vec{S} \tag{2.8}$$

The conservative variable vector, $\vec{U}$ is defined as:

$$\vec{U} = \begin{vmatrix} \rho \\ \rho u \\ \rho v \\ \rho w \\ \rho E \end{vmatrix} \tag{2.9}$$

The flux vectors, $\vec{E}$, $\vec{F}$ and $\vec{G}$ can be split into inviscid and viscous fluxes as follows:

$$\vec{E} = \vec{E_i} - \vec{E_v} = \begin{vmatrix} \rho u \\ \rho u^2 + p \\ \rho v u \\ \rho w u \\ \rho H u \end{vmatrix} - \begin{vmatrix} 0 \\ \tau_{xx} \\ \tau_{yx} \\ \tau_{zx} \\ u\tau_{xx} + v\tau_{yx} + w\tau_{zx} \end{vmatrix} \tag{2.10}$$

$$\vec{F} = \vec{F_i} - \vec{F_v} = \begin{vmatrix} \rho v \\ \rho u v \\ \rho v^2 + p \\ \rho w v \\ \rho H v \end{vmatrix} - \begin{vmatrix} 0 \\ \tau_{xy} \\ \tau_{yy} \\ \tau_{zy} \\ u\tau_{xy} + v\tau_{yy} + w\tau_{zy} \end{vmatrix} \tag{2.11}$$

$$\vec{G} = \vec{G_i} - \vec{G_v} = \begin{vmatrix} \rho w \\ \rho u w \\ \rho v w \\ \rho w^2 + p \\ \rho H w \end{vmatrix} - \begin{vmatrix} 0 \\ \tau_{xz} \\ \tau_{yz} \\ \tau_{zz} \\ u\tau_{xz} + v\tau_{yz} + w\tau_{zz} \end{vmatrix} \tag{2.12}$$

The ideal gas equation is used to relate thermodynamic quantities:

$$p = \rho R T \tag{2.13}$$

For the turbulent calculations in this study, the standard compressible Navier-Stokes equations as presented in this section are not solved. Instead, the Reynolds-averaged form of the Navier-Stokes equations are solved in the RANS section and the filtered Navier-Stokes equations are solved in the LES section.

2.2 Filtered Navier-Stokes Equations

Large Eddy Simulation models require filtering of the governing equations into a resolvable-scale components and subgrid-scale (SGS) components. For a generic property A:

$$A = \bar{A} + A' \tag{2.14}$$

where $\bar{A}$ is the filtered component of the property. A generic filter is of the form [4]:

$$\bar{A}_i\left(x_i,\, t\right) = \int\int\int G\left(x_i - \xi_i,\, \Delta\right) A_i\left(\xi_i,\, \Delta\right) d^3\xi_i \tag{2.15}$$

The filter function is normalized as follows:

$$\int\int\int G\left(x_i - \xi_i,\, \Delta\right) d^3\xi_i = 1 \tag{2.16}$$

where

$$\Delta = \sqrt[3]{\Delta_x \Delta_y \Delta_z} \tag{2.17}$$

The filtered forms of the Navier-Stokes equations are as follows:

$$\frac{\partial \bar{\rho}}{\partial t} + \frac{\partial}{\partial x_i}\left(\bar{\rho}\bar{u_i}\right) = 0 \tag{2.18}$$

$$\frac{\partial}{\partial t}\left(\bar{\rho}\tilde{u_i}\right) + \frac{\partial}{\partial x_j}\left(\bar{\rho}\tilde{u_i}\tilde{u_j}\right) = -\frac{\partial \bar{p}}{\partial x_i} + \frac{\partial}{\partial x_j}\left(\tau_{ij} + \tau_{ij}^S\right) \tag{2.19}$$

$$\frac{\partial}{\partial t}\left(\bar{\rho}\tilde{E}\right) + \frac{\partial}{\partial x_j}\left(\bar{\rho}\tilde{H}\tilde{u_j}\right) = \frac{\partial}{\partial x_j}\left[\tilde{u_i}\left(\tau_{ij} + \tau_{ij}^S\right) - \left(q_j + Q_j\right)\right] \tag{2.20}$$

where filtered pressure is $\bar{p} = \bar{\rho}R\tilde{T}$. The filtered total energy and total enthalpy, $\tilde{E}$ and $\tilde{H}$

are as follows:

$$\tilde{E} = C_v\tilde{T} + \frac{1}{2}\tilde{u_i}\tilde{u_i} + k \tag{2.21}$$

$$\tilde{H} = C_p\tilde{T} + \frac{1}{2}\tilde{u_i}\tilde{u_i} + k \tag{2.22}$$

where k is the subgrid scale turbulent kinetic energy per unit mass:

$$k = \frac{1}{2}\left(\widetilde{u_i u_j} - \tilde{u_i}\tilde{u_j}\right) \tag{2.23}$$

The Boussinesq eddy viscosity approximation and the gradient-diffusion approximation are typically used to calculate the Reynolds stresses and subgrid-scale heat flux:

$$\tau_{ij}^S = \mu_t\left(\frac{\partial\tilde{u}_i}{\partial x_j} + \frac{\partial\tilde{u}_j}{\partial x_i} - \frac{2}{3}\frac{\partial\tilde{u}_k}{\partial x_k}\delta_{ij}\right) \tag{2.24}$$

$$Q_j = -\frac{\mu_t C_p}{Pr_t}\frac{\partial\tilde{T}}{\partial x_j} \tag{2.25}$$

where μ_T is the eddy viscosity and is determined by the turbulence model that is used.

Turbulence Closure

Most simply, in LES the large scale eddies are computed and the eddies smaller than the SGS eddies are modeled. Because LES simulations directly calculate the larger fluctuations and leave modeling only for SGS fluctuations, it is far more versatile than methods that rely solely on modeling of turbulent fluctuations. Because the smallest fluctuations are modeled, cells and time steps can be much larger than DNS simulations.

The Yoshizawa [26] one equation subgrid model based on solving for turbulent kinetic energy is used.

$$\rho\frac{\mathrm{D}k}{\mathrm{D}t} = P_k - \rho C_d\frac{k^{\frac{3}{2}}}{\Delta} + \frac{\partial}{\partial x_j}\left[\left(\mu + \mu_t\right)\frac{\partial k}{\partial x_j}\right] \tag{2.26}$$

where

$$\mu_t = \rho C_s\sqrt{k}\Delta \tag{2.27}$$

The model constants used by Yoshizawa were slightly altered in order to set $C_d = 1.0$ and $C_{smag} = 0.1$, and using the following equation [26]:

$$C_{smag} = \left(\frac{C_s^3}{C_d}\right)^{\frac{1}{4}} \tag{2.28}$$

A value of 0.04641 for C_s satisfies that relation.

2.3 Reynolds-averaged Navier-Stokes Equations

The Reynolds-averaged Navier-Stokes equations facilitate turbulent averaging in order to model the temporal fluctuations due to turbulence and effectively remove them without removing other time-dependent aspects of the flow. For a generic quantity A, its value can be equated to the sum of a time-averaged quantity $\bar{A}$ and a fluctuation in that property A':

$$A = \bar{A} + A' \tag{2.29}$$

The time-averaged quantity $\bar{A}$ can be calculated over the time period $\mathcal{T}$ with:

$$\bar{A} = \frac{1}{\mathcal{T}} \int_{-\mathcal{T}/2}^{\mathcal{T}/2} A(\vec{x}, t+\tau)\, dt \tag{2.30}$$

For compressible flows, such as the one in question in this study, this averaging can cause fluctuations between density and other flow variables. In order to avoid these explicit fluctuations, density-averaging [27] can be used:

$$\tilde{A} = \frac{\overline{\rho A}}{\bar{\rho}} \tag{2.31}$$

where

$$A = \tilde{A} + A'' \tag{2.32}$$

and

$$\overline{\rho A''} = 0 \tag{2.33}$$

When using this averaging process, known as Favre averaging, the Navier-Stokes equations

are in the same form as the filtered Navier-Stokes Equations:

$$\frac{\partial \bar{\rho}}{\partial t} + \frac{\partial}{\partial x_i}\left(\bar{\rho}\bar{u_i}\right) = 0 \tag{2.34}$$

$$\frac{\partial}{\partial t}\left(\bar{\rho}\tilde{u_i}\right) + \frac{\partial}{\partial x_j}\left(\bar{\rho}\tilde{u_i}\tilde{u_j}\right) = -\frac{\partial \bar{p}}{\partial x_i} + \frac{\partial}{\partial x_j}\left(\tau_{ij} + \tau_{ij}^R\right) \tag{2.35}$$

$$\frac{\partial}{\partial t}\left(\bar{\rho}\tilde{E}\right) + \frac{\partial}{\partial x_j}\left(\bar{\rho}\tilde{H}\tilde{u_j}\right) = \frac{\partial}{\partial x_j}\left[\tilde{u_i}\left(\tau_{ij} + \tau_{ij}^R\right) - \left(q_j + Q_j\right)\right] \tag{2.36}$$

The momentum equation requires defining a Reynolds stress term, τ_{ij}^R and the turbulent heat flux:

$$\tau_{ij}^R = -\bar{\rho}\overline{u_i'' u_j''} \tag{2.37}$$

$$Q_j = \overline{\rho u_j'' h''} \tag{2.38}$$

The same approximation can be made for heat flux as with the LES (Eq. 2.25).

For this study the two-equation turbulence model developed by Menter [12] was used. Two variations (Menter BSL and Menter SST) were used for turbulence closure.

Menter BSL Turbulence Closure

Menter's model was used as a turbulence closure model for the RANS simulation in this study. The Menter Baseline model (Menter BSL) is a two-equation model [12] that uses Wilcox's k-ω model [4] near the wall and the k-ϵ model in the outer part of the boundary later. This is achieved by transforming the k-ϵ model into a k-ω form and employing a blending function to transition between the two. This allows for the use of the Wilcox k-ω near the wall with its ability to model viscous wall-bounded flows. The k-ϵ model can be used away from the wall where the k-ω model has been shown to be very sensitive to ω freestream conditions [28]. The only difference between the transformed k-ϵ model and the k-ω model is the addition of a cross-diffusion term in the ω equation:

Original k-ω model:

$$\frac{\mathrm{D}\rho k}{\mathrm{D}t} = \tau_{ij}\frac{\partial u_i}{\partial x_j} - \beta^*\rho\omega k + \frac{\partial}{\partial x_j}\left[\left(\mu + \sigma_{k1}\mu_t\right)\frac{\partial k}{\partial x_j}\right] \tag{2.39}$$

$$\frac{\mathrm{D}\rho\omega}{\mathrm{D}t} = \frac{\gamma_1}{\nu_t}\tau_{ij}\frac{\partial u_i}{\partial x_j} - \beta_1\rho\omega^2 + \frac{\partial}{\partial x_j}\left[(\mu + \sigma_{\omega 1}\mu_t)\frac{\partial \omega}{\partial x_j}\right] \tag{2.40}$$

Transformed k-ϵ model:

$$\frac{\mathrm{D}\rho k}{\mathrm{D}t} = \tau_{ij}\frac{\partial u_i}{\partial x_j} - \beta^*\rho\omega k + \frac{\partial}{\partial x_j}\left[(\mu + \sigma_{k2}\mu_t)\frac{\partial k}{\partial x_j}\right] \tag{2.41}$$

$$\frac{\mathrm{D}\rho\omega}{\mathrm{D}t} = \frac{\gamma_2}{\nu_t}\tau_{ij}\frac{\partial u_i}{\partial x_j} - \beta_2\rho\omega^2 + \frac{\partial}{\partial x_j}\left[(\mu + \sigma_{\omega 2}\mu_t)\frac{\partial \omega}{\partial x_j}\right] + 2\rho\sigma_{\omega 2}\frac{1}{\omega}\frac{\partial k}{\partial x_j}\frac{\partial \omega}{\partial x_j} \tag{2.42}$$

Equations 2.39 and 2.40 are then multiplied by a blending function F1 and Equations 2.41 and 2.42 are multiplied by (1-F1) and the two equations are added together. The combined equations are as follows:

$$\rho\frac{\mathrm{D}k}{\mathrm{D}t} = P_k - \rho\beta_* k\omega + \frac{\partial}{\partial x_j}\left[(\mu + \mu_t)\frac{\partial k}{\partial x_j}\right] \tag{2.43}$$

$$\frac{\mathrm{D}\rho\omega}{\mathrm{D}t} = P_\omega - \beta\rho\omega^2 + \frac{\partial}{\partial x_j}\left[(\mu + \sigma_\omega\mu_t)\frac{\partial \omega}{\partial x_j}\right] + 2\left(1 - F_1\right)\rho\sigma_{\omega 2}\frac{1}{\omega}\frac{\partial k}{\partial x_j}\frac{\partial \omega}{\partial x_j} \tag{2.44}$$

where:

$$P_k \equiv \mu_t S^2 \tag{2.45}$$

$$\mu_t = \rho\nu_t = \rho\frac{k}{\omega} \tag{2.46}$$

and

$$S = \left[\frac{\partial \vec{u_i}}{\partial x_j}\frac{\partial \vec{u_j}}{\partial x_i} + \frac{\partial \vec{u_i}}{\partial x_j}\frac{\partial \vec{u_i}}{\partial x_j} - \frac{2}{3}\left(\frac{\partial \vec{u_i}}{x_i}\right)^2\right]^{\frac{1}{2}} \tag{2.47}$$

The blending function F_1 is given by:

$$F_1 = \tanh\left(\arg_1^4\right) \tag{2.48}$$

Table 2.1: Model constants for Menter BSL and SST

Model Constant	(inner) BSL (Wilcox)	(outer) k-ϵ	(inner) SST (Menter)
σ_k	0.5	1.0	0.81
σ_ω	0.5	0.856	0.5
β	0.0750	0.0828	0.0750
β^*	0.09	0.09	0.09
γ	0.5532	0.4404	0.5532

$$\arg_1 = \min\left[\max\left(\frac{\sqrt{k}}{0.09\omega y}; \frac{4\rho\sigma_{\omega 2}k}{\mathrm{CD}_{k\omega}y^2}\right)\right] \tag{2.49}$$

where y is the distance to the nearest surface and $\mathrm{CD}_{k\omega}$ is as follows:

$$\mathrm{CD}_{k\omega} = \max\left(2\rho\sigma_{\omega 2}\frac{1}{\omega}\frac{\partial k}{\partial x_j}\frac{\partial \omega}{\partial x_j}, 10^{-20}\right) \tag{2.50}$$

The model constants between the transformed k-ϵ and k-ω equations must be blended in the same way, with ϕ_1 indicating an inner (Wilcox $k-\omega$) value and ϕ_2 indicating an outer ($k-\epsilon$) value:

$$\phi = F_1\phi_1 + (1 - F_1)\phi_2 \tag{2.51}$$

The model constants for k-ϵ and Wilcox's k-ω can be found in Table 2.1.

Menter SST Turbulence Closure

Menter showed that his shear stress transport model was an improvement over the Menter baseline model and other two-equation turbulence models [12]. The SST model improves performance for adverse pressure gradient flows. It does so by accounting for the transport of the principal turbulent shear stress by including the term:

$$\frac{\mathrm{D}\tau}{\mathrm{D}t} = \frac{\partial \tau}{\partial t} + u_k\frac{\partial \tau}{\partial x_k} \tag{2.52}$$

Menter's implementation of this term into his two-equation model stemmed from the Johnson-King algebraic model [29]. The Johnson-King model uses the Bradshaw assumption [30] that shear stress in a boundary layer is proportional to the turbulent kinetic

energy, k (with $a_1 = 0.31$):

$$\tau = \rho a_1 k \tag{2.53}$$

Whereas, standard two-equation models use the following definition for shear stress:

$$\tau = \mu_t \Omega \tag{2.54}$$

where $\Omega = (\partial u/\partial y)$. Menter re-worked this equation to be used in his eddy viscosity model by redefining the eddy viscosity as follows:

$$\nu_t = \frac{Ak}{\max(A\omega; SF_2)} \tag{2.55}$$

This equation makes use of a blending function, F_2, such that the use of Bradshaw's assumption is limited to wall-bounded flows:

$$F_2 = \tanh(arg_2^2) \tag{2.56}$$

$$arg_2 = \max\left(2\frac{\sqrt{k}}{0.09\omega y}; \frac{500\nu}{y^2\omega}\right) \tag{2.57}$$

Some of the model constants must be adjusted for the shear stress transport modification. These values can be found in Table 2.1.

2.4 Hybrid LES/RANS model

The hybrid flow solver combines the Menter-closed RANS model and the Yoshizawa one-equation model in the transport equation for turbulent kinetic energy:

$$\rho\frac{\mathrm{D}k}{\mathrm{D}t} = P_k - \rho\left[\Gamma\beta_* k\omega + (1-\Gamma)\, C_d \frac{k^{\frac{3}{2}}}{\Delta}\right] + \frac{\partial}{\partial x_j}\left[(\mu + \mu_t)\frac{\partial k}{\partial x_j}\right] \tag{2.58}$$

where:

$$P_k \equiv \mu_t S^2 \tag{2.59}$$

$$\mu_t = \rho\nu_t = \rho\left[\Gamma\frac{k}{\tilde{\omega}} + (1-\Gamma)\,C_s\sqrt{k}\Delta\right] \tag{2.60}$$

and

$$S = \left[\frac{\partial\vec{u_i}}{\partial x_j}\frac{\partial\vec{u_j}}{\partial x_i} + \frac{\partial\vec{u_i}}{\partial x_j}\frac{\partial\vec{u_i}}{\partial x_j} - \frac{2}{3}\left(\frac{\partial\vec{u_i}}{x_i}\right)^2\right]^{\frac{1}{2}} \tag{2.61}$$

$$\Delta = \sqrt[3]{\Delta_x\Delta_y\Delta_z} \tag{2.62}$$

In Eq. 2.60 $\tilde{\omega}$ represents the turbulence frequency as modified by the SST:

$$\tilde{\omega} = \max\left(\omega,\ \frac{F_2 S}{A}\right) \tag{2.63}$$

When the Menter BSL model is used, ω can be substituted for $\tilde{\omega}$. The equation for turbulence frequency is in the Menter form, without any direct influence from the hybrid blending function, Γ:

$$\frac{\mathrm{D}\rho\omega}{\mathrm{D}t} = P_\omega - \beta\rho\omega^2 + \frac{\partial}{\partial x_j}\left[(\mu + \sigma_\omega\mu_t)\frac{\partial\omega}{\partial x_j}\right] + 2\,(1-F_1)\,\rho\sigma_{\omega 2}\frac{1}{\omega}\frac{\partial k}{\partial x_j}\frac{\partial\omega}{\partial x_j} \tag{2.64}$$

where the production term, P_k and P_ω were modified so that they were limited to no greater than 25 times their destruction terms:

$$P_k = \min\left(\mu_t S^2,\ 25\beta^*\rho k\omega\right) \tag{2.65}$$

$$P_\omega = \min\left(\gamma\rho S^2,\ 25\beta\rho\omega^2\right) \tag{2.66}$$

Equations 2.58 and 2.64 combined with the filtered Navier-Stokes equations (Eqs. 2.18-2.20) (noting the difference in the calculation of Reynolds stress versus sugrid stress for the RANS model) make up the full equation set. When the assumptions which have been detailed in the preceding sections are applied, the model is closed. For a complete set of model constants used, see Appendix A.

Blending Function

The blending function is based on a ratio of the closest wall distance d to a modeled form of the Taylor microscale, λ:

$$\Gamma = \frac{1}{2}\left\{1 - \tanh\left[5\left(\frac{\kappa}{\sqrt{C_\mu}}\eta^2 - 1\right) + \phi\right]\right\} \tag{2.67}$$

where:

$$\eta = \frac{d}{A\lambda} \tag{2.68}$$

The ϕ term is used to set the value for the blending function where the LES and RANS contributions are equal. For this study a value of 0.0 was used throughout (which translates into an equal contribution at $\Gamma = 0.5$). With this form of blending function, the physical location of this point can be shifted easily by changing the value of A. Using the log-law expression $\omega = u_\tau/\sqrt{\beta_*}\kappa d$ in the equation for Taylor microscale, it can be shown that:

$$\lambda = \sqrt{\frac{\nu}{C_\mu \omega}} \tag{2.69}$$

When this form is used, an estimation for the RANS/LES juncture (defined as $\Gamma = 0.5$) can be made using the wall coordinate d^+. Using log-law expressions it can be shown that $d^+ = A^2$ at the RANS/LES juncture (see Appendix B).

Chapter 3

Numerical Methods

3.1 Coordinate Transformation

The governing equations are solved in a computational space that is transformed from the Cartesian space. In order to use the Navier-Stokes equations in computational space, the following transformation is used:

$$\begin{aligned} \xi &= \xi(x, y, z) \\ \eta &= \eta(x, y, z) \\ \zeta &= \zeta(x, y, z) \end{aligned} \tag{3.1}$$

The Navier-Stokes equations were converted into computational space. Equation 2.1 can be rewritten as follows:

$$\frac{\partial \vec{\mathcal{U}}}{\partial t} + \frac{\partial \vec{\mathcal{E}} - \vec{\mathcal{E}}_v}{\partial \xi} + \frac{\partial \vec{\mathcal{F}} - \vec{\mathcal{F}}_v}{\partial \eta} + \frac{\partial \vec{\mathcal{G}} - \vec{\mathcal{G}}_v}{\partial \zeta} \tag{3.2}$$

The conservative variable vector can be written:

$$\vec{\mathcal{U}} = \frac{1}{J}\begin{vmatrix} \tilde{\rho} \\ \tilde{\rho}\tilde{u} \\ \tilde{\rho}\tilde{v} \\ \tilde{\rho}\tilde{w} \\ \tilde{\rho}\tilde{E}_t \\ \tilde{\rho}k \\ \tilde{\rho}\omega \end{vmatrix} \tag{3.3}$$

The inviscid fluxes can be rewritten as follows:

$$\vec{\mathcal{E}} = \frac{1}{J}\begin{vmatrix} \bar{\rho}\tilde{\mathcal{U}} \\ \bar{\rho}\tilde{u}\tilde{\mathcal{U}} + \xi_x\bar{p} \\ \bar{\rho}\tilde{v}\tilde{\mathcal{U}} + \xi_y\bar{p} \\ \bar{\rho}\tilde{w}\tilde{\mathcal{U}} + \xi_z\bar{p} \\ \bar{\rho}\tilde{h}_t\tilde{\mathcal{U}} \\ \bar{\rho}k\tilde{\mathcal{U}} \\ \bar{\rho}\omega\tilde{\mathcal{U}} \end{vmatrix} \quad \vec{\mathcal{F}} = \frac{1}{J}\begin{vmatrix} \bar{\rho}\tilde{\mathcal{V}} \\ \bar{\rho}\tilde{u}\tilde{\mathcal{V}} + \eta_x\bar{p} \\ \bar{\rho}\tilde{v}\tilde{\mathcal{V}} + \eta_y\bar{p} \\ \bar{\rho}\tilde{w}\tilde{\mathcal{V}} + \eta_z\bar{p} \\ \bar{\rho}\tilde{h}_t\tilde{\mathcal{V}} \\ \bar{\rho}k\tilde{\mathcal{V}} \\ \bar{\rho}\omega\tilde{\mathcal{V}} \end{vmatrix} \quad \vec{\mathcal{G}} = \frac{1}{J}\begin{vmatrix} \bar{\rho}\tilde{\mathcal{W}} \\ \bar{\rho}\tilde{u}\tilde{\mathcal{W}} + \zeta_x\bar{p} \\ \bar{\rho}\tilde{v}\tilde{\mathcal{W}} + \zeta_y\bar{p} \\ \bar{\rho}\tilde{w}\tilde{\mathcal{W}} + \zeta_z\bar{p} \\ \bar{\rho}\tilde{h}_t\tilde{\mathcal{W}} \\ \bar{\rho}k\tilde{\mathcal{W}} \\ \bar{\rho}\omega\tilde{\mathcal{W}} \end{vmatrix} \tag{3.4}$$

The viscous fluxes are as follows:

$$\vec{\mathcal{E}}_v = \frac{1}{J}\begin{vmatrix} 0 \\ \xi_{x_i}\left(\tau_{i1} + \tau'_{i1}\right) \\ \xi_{x_i}\left(\tau_{i2} + \tau'_{i2}\right) \\ \xi_{x_i}\left(\tau_{i3} + \tau'_{i3}\right) \\ \xi_{x_i}\left[\tilde{u}_j\left(\tau_{ij} + \tau'_{ij}\right) - q_i + q'_i\right] \\ \xi_{x_i}\left(\mu + \sigma_k\mu_t\right)\left|\nabla\xi\right|^2\frac{\partial k}{\partial x_i} \\ \xi_{x_i}\left(\mu + \sigma_\omega\mu_t\right)\left|\nabla\xi\right|^2\frac{\partial \omega}{\partial x_i} \end{vmatrix} \tag{3.5}$$

$$\vec{\mathcal{F}}_v = \frac{1}{J}\begin{vmatrix} 0 \\ \eta_{x_i}\left(\tau_{i1}+\tau'_{i1}\right) \\ \eta_{x_i}\left(\tau_{i2}+\tau'_{i2}\right) \\ \eta_{x_i}\left(\tau_{i3}+\tau'_{i3}\right) \\ \eta_{x_i}\left[\tilde{u}_j\left(\tau_{ij}+\tau'_{ij}\right)-q_i+q'_i\right] \\ \eta_{x_i}\left(\mu+\sigma_k\mu_t\right)\left|\nabla\eta\right|^2\frac{\partial k}{\partial x_i} \\ \eta_{x_i}\left(\mu+\sigma_\omega\mu_t\right)\left|\nabla\eta\right|^2\frac{\partial \omega}{\partial x_i} \end{vmatrix} \tag{3.6}$$

$$\vec{\mathcal{G}}_v = \frac{1}{J}\begin{vmatrix} 0 \\ \zeta_{x_i}\left(\tau_{i1}+\tau'_{i1}\right) \\ \zeta_{x_i}\left(\tau_{i2}+\tau'_{i2}\right) \\ \zeta_{x_i}\left(\tau_{i3}+\tau'_{i3}\right) \\ \zeta_{x_i}\left[\tilde{u}_j\left(\tau_{ij}+\tau'_{ij}\right)-q_i+q'_i\right] \\ \zeta_{x_i}\left(\mu+\sigma_k\mu_t\right)\left|\nabla\zeta\right|^2\frac{\partial k}{\partial x_i} \\ \zeta_{x_i}\left(\mu+\sigma_\omega\mu_t\right)\left|\nabla\zeta\right|^2\frac{\partial \omega}{\partial x_i} \end{vmatrix} \tag{3.7}$$

where σ_k and σ_ω are calculated using the Menter blending function as in Eq. 2.51. The contravariant velocities used above can be calculated as follows:

$$\begin{aligned} \tilde{\mathcal{U}} &\equiv \xi_x\tilde{u}+\xi_y\tilde{v}+\xi_z\tilde{w} \\ \tilde{\mathcal{V}} &\equiv \eta_x\tilde{u}+\eta_y\tilde{v}+\eta_z\tilde{w} \\ \tilde{\mathcal{W}} &\equiv \zeta_x\tilde{u}+\zeta_y\tilde{v}+\zeta_z\tilde{w} \end{aligned} \tag{3.8}$$

and the Jacobian, J can be defined as follows:

$$J = \begin{vmatrix} \xi_x & \xi_y & \xi_z \\ \eta_x & \eta_y & \eta_z \\ \zeta_x & \zeta_y & \zeta_z \end{vmatrix} \tag{3.9}$$

3.2 Low-Diffusion Flux Splitting Scheme

Edwards' LDFSS(2) [31] is used for the inviscid fluxes. The scheme requires that the flux be split into pressure and convective components. For illustrative purposes, only

the flux in the ξ direction is shown:

$$\vec{\mathcal{E}} = \vec{\mathcal{E}}^c + \vec{\mathcal{E}}^v = \frac{1}{J}\left(\rho \mathcal{U} \vec{E}^c + p\vec{E}^p\right) \tag{3.10}$$

$$\vec{E}^c = \begin{vmatrix} 1 \\ u \\ v \\ w \\ h_t \\ k \\ \omega \end{vmatrix} \quad , \quad \vec{E}^p = \begin{vmatrix} 0 \\ \xi_x \\ \xi_y \\ \xi_z \\ 0 \\ 0 \\ 0 \end{vmatrix} \tag{3.11}$$

The convective fluxes are defined as:

$$\vec{\mathcal{E}}^c_{1/2} = \frac{|\nabla \xi|}{J} a_{1/2}\left(\rho_L C^+ \vec{E}^c_L + \rho_R C^- \vec{E}^c_R\right) \tag{3.12}$$

where the interface sound speed, $a_{1/2}$ is defined as follows:

$$a_{1/2} = \frac{1}{2}\left(a_L + a_R\right) \tag{3.13}$$

and

$$C^+ = C^+_{VL} - M^+_{1/2} \tag{3.14}$$

$$C^- = C^-_{VL} - M^-_{1/2} \tag{3.15}$$

where

$$C^+_{VL} = \alpha^+_L\left(1.0 + \beta_L\right) M_L - \beta_L M^+_L \tag{3.16}$$

$$C^-_{VL} = \alpha^-_R\left(1.0 + \beta_R\right) M_R - \beta_R M^+_R \tag{3.17}$$

$$M_{1/2}^{+} = M_{1/2}\left(\frac{2p_R}{p_L + p_R} - \delta\frac{|p_L - p_R|}{p_L}\right) \tag{3.18}$$

$$M_{1/2}^{-} = M_{1/2}\left(\frac{2p_L}{p_L + p_R} - \delta\frac{|p_L - p_R|}{p_R}\right) \tag{3.19}$$

and

$$\alpha_{L,R}^{\pm} = \frac{1}{2}\left[1.0 \pm \mathtt{sign}\left(M_{L,R}\right)\right] \tag{3.20}$$

$$\beta_{L,R} = -\max\left[0.0,\ 1.0 - \mathtt{int}\left(|M_{L,R}|\right)\right] \tag{3.21}$$

$$M_{1/2} = \frac{\beta_L\beta_R}{4}\left[\sqrt{\frac{1}{2}\left(M_L^2 + M_R^2\right)} - 1.0\right]^2 \tag{3.22}$$

The left and right Mach numbers are defined using the interface sound speed:

$$M_{L,R} = \frac{\xi_x u_{L,R} + \xi_y v_{L,R} + \xi_z w_{L,R}}{a_{1/2}\left|\nabla\xi\right|} \tag{3.23}$$

$$p_{L,R}^{\pm} = \frac{1}{4}\left(M_{L,R} \pm 1.0\right)^2\left(2.0 \mp M_{L,R}\right) \tag{3.24}$$

This numerical scheme was extended to second-order spatial accuracy using the SONIC-A ENO scheme as derived in Ref. [32]. For the purposes of this description, let the symbol ϕ_i denote any primitive variable (ρ,u,v,w,T,k and ω were extrapolated in this simulation). The higher-order extension is implemented using a monotone interpolation as follows:

$$\phi_{i-1/2}^{+} = \phi_i + a_i\left(x_{i+1/2} - x_i\right) \tag{3.25}$$

$$\phi_{i+1/2}^{-} = \phi_i + a_i\left(x_{i-1/2} - x_i\right) \tag{3.26}$$

where, for the SONIC-A scheme:

$$a_i = \mathtt{sign}\left(t_i\right)\min\left[\frac{\left|\left(t_i^{-} + t_i^{+}\right)\right|}{2}, \max\left(2|s_i|, |t_i|\right)\right] \tag{3.27}$$

where:

$$t_i^- = s_{i-1/2} + d_{i-1/2}\Delta x \tag{3.28}$$

$$t_i^+ = s_{i+1/2} - d_{i+1/2}\Delta x \tag{3.29}$$

$$t_i = \text{minmod}\left(t_i^-, t_i^+\right) \tag{3.30}$$

$$s_i = \frac{1}{2}\texttt{sign}\left(s_{i+1/2} + s_{i-1/2}\right)\min\left(\left|s_{i+1/2}\right|,\ \left|s_{i-1/2}\right|\right) \tag{3.31}$$

where $s_{i+1/2}$ and $s_{i-1/2}$ signify linear slopes:

$$s_{i+1/2} = \frac{\phi_{i+1} - \phi_i}{\Delta x} \tag{3.32}$$

$$s_{i-1/2} = \frac{\phi_i - \phi_{i-1}}{\Delta x} \tag{3.33}$$

and $d_{i+1/2}$ and $d_{i-1/2}$ are defined as follows:

$$d_i = \frac{\phi_{i+1} - 2\phi_i + \phi_{i-1}}{\Delta x^2} \tag{3.34}$$

$$d_{i+1/2} = \text{minmod}\left(d_i,\ d_{i+1}\right) \tag{3.35}$$

$$d_{i-1/2} = \text{minmod}\left(d_i,\ d_{i-1}\right) \tag{3.36}$$

These 1-D definitions can be similarly implemented in the j and k directions since there are no cross terms in the monotone interpolation. In some cases where dispersion was a problem near the walls, the more dissipative Van Albada limiter [33] was used for a few iterations to damp out these problems.

3.3 Time Integration

Second-order temporal accuracy was achieved through the use of a planar relaxation sub-iteration procedure and the Crank-Nicholson time discretization. A Crank-Nicholson discretization was used in time to form the unsteady residual, $\mathcal{R}$:

$$\mathcal{R}^{n+1,k} = -\frac{U^{n+1,k} - U^n}{\Delta t} + \frac{1}{2}\left(R\left(U^{n+1,k}\right) + R\left(U^n\right)\right) \tag{3.37}$$

In Eq. 3.37, the n and $n+1$ superscripts represent the current and next time level. The k superscript represents the current subiteration level. For each time level the solution was iterated in k to a desired convergence or number of subiterations. The solution, in primitive variables, was updated at the subiteration level as follows for a single grid point [34]:

$$\begin{aligned} -\mathcal{R}^{n+1,k}_{i,j,k} \;=\; & \left[\frac{1}{\Delta t}\frac{\partial U}{\partial V} + \frac{1}{2}\left(\tilde{A} - \frac{\partial S}{\partial V}\right)\right]^{n+1,k}_{i,j,k} \Delta V^{n+1,k+1}_{i,j,k} + \\ & \frac{1}{2}\tilde{B}\Delta V^{n+1,k+1}_{i,j-1,k} + \frac{1}{2}\tilde{C}\Delta V^{n+1,k+1}_{i,j+1,k} + \\ & \frac{1}{2}\tilde{D}\Delta V^{n+1,k+1}_{i,j,k-1} + \frac{1}{2}\tilde{E}\Delta V^{n+1,k+1}_{i,j,k+1} + \\ & \frac{1}{2}\tilde{F}\Delta V^{n+1,k+1}_{i-1,j,k} + \frac{1}{2}\tilde{G}\Delta V^{n+1,k+1}_{i+1,j,k} \end{aligned} \tag{3.38}$$

Details on the calculations of the flux Jacobians $\tilde{A}$ - $\tilde{G}$ can be found in [31]. The implicit calculation of the system Jacobian matrix $\tilde{A}$ in Eqn. 3.38 is approximated by a symmetric planar Gauss-Seidel (SPGS) algorithm. First matrix elements in the same $i = const$ plane are denoted as D as shown in Ref. [35]:

$$D = \frac{1}{\Delta t}\frac{\partial U}{\partial V} + \frac{1}{2}\left(\tilde{A} - \frac{\partial S}{\partial V} + \tilde{B} + \tilde{C} + \tilde{D} + \tilde{E}\right) \tag{3.39}$$

The off-plane components can be grouped as follows:

$$L = \tilde{F} \tag{3.40}$$

$$U = \tilde{G} \tag{3.41}$$

Then Eqn. 3.38 can be reduced using SPGS as follows:

$$(D+L)^{n+1,k}\left(D^{n+1,k}\right)^{-1}(D+U)^{n+1,k}\,\Delta\vec{V}^{n+1,k+1} = -\mathcal{R}^{n+1,k} \tag{3.42}$$

This algorithm was implemented by using a forward and backward sweep in the ξ direction:

$$\textbf{forward}: \quad \Delta\vec{V}_i^{n+1,k+1/2} = \left(D_i^{n+1,k}\right)^{-1}\left(-\mathcal{R}_i^{n+1,k} - L_{i-1}^{n+1,k}\Delta\vec{V}_{i-1}^{n+1,k+1/2}\right) \tag{3.43}$$

$$\textbf{backward}: \quad \Delta\vec{V}_i^{n+1,k+1} = \Delta\vec{V}_i^{n+1,k+1/2} - \left(D_i^{n+1,k}\right)^{-1}U_{i+1}^{n+1,k}\Delta\vec{V}_{i+1}^{n+1,k+1} \tag{3.44}$$

The block pentadiagonal matrix was solved using an ILU factorization. The primitive variables was then updated as follows:

$$\vec{V}^{n+1,k+1} = \vec{V}^{n+1,k} + \Delta\vec{V}^{n+1,k+1} \tag{3.45}$$

3.4 Recycling Procedure

The simulation used a recycling and rescaling procedure to initiate and sustain large-scale turbulent structures in the flat-plate inflow region of the domain. This was achieved by separating the fluctuating and mean components of the flow properties (u, v, w, T and P) at a specified recycle plane downstream of the inflow plane. The fluctuating components were then scaled and super-imposed onto a RANS mean inflow. For the turbulent quantities k, ω and μ_T, the property itself is imposed on the inflow plane. For a generic property q, the fluctuating and mean components (denoted as q' and $\bar{q}$, respectively) can be found as follows:

$$\bar{q} = \frac{1}{t_f - t_i}\int_{t_i}^{t_f} q\,dt \tag{3.46}$$

$$q' = q - \bar{q} \tag{3.47}$$

In order to avoid imposing the freestream property fluctuations from the recycle plane onto the inlet plane, a function based on y/δ (denoted here as f) was used. It does so by reducing the influence of the fluctuations of velocity, temperature and pressure on the

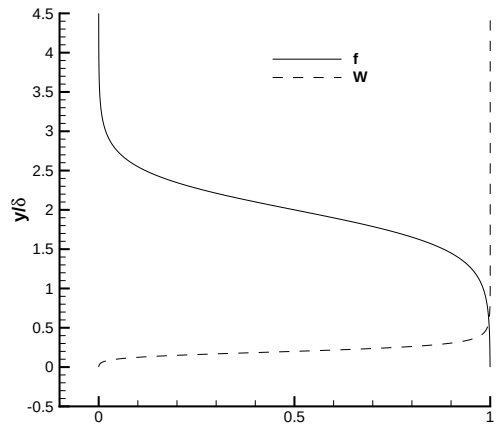

Figure 3.1: Blending functions for recycling/rescaling procedure

inlet flow away from the edge of the boundary layer. This procedure allowed for the RANS mean inflow to be maintained in the freestream.

$$q_{inl} = q_{RANS} + f q'_{resc} \tag{3.48}$$

For the turbulent properties k, ω, and μ_T, the same function is used to blend from the rescaled property to the RANS mean inflow property:

$$q_{inl} = (1 - f)\, q_{RANS} + f q_{resc} \tag{3.49}$$

where

$$f = \frac{1}{2}\left[1 - \tanh\left(2\frac{y_{inl}}{\delta_{inl}} - 4\right)\right] \tag{3.50}$$

The variables q'_{resc} and q_{resc} represent the rescaled fluctuation of a property and the rescaled property, respectively. A plot for Eqn. 3.50 can be found in Fig. 3.1. The transition point of the function ($f = 0.5$) occurs at twice the imposed boundary layer thickness at the inflow plane ($y = 4.130cm$). The rescaling of properties (for turbulent properties) and property fluctuations (for other properties) is handled differently between the inner and outer parts of boundary layer. This is accomplished by using a blending function, W (also shown in Fig. 3.1) in the following way:

$$q_{resc} = q_{rec}\left(\frac{y_{inl}}{R_\beta}\right)(1-W) + q_{rec}\left(y_{inl}R_\delta\right)W \tag{3.51}$$

$$q'_{resc} = q'_{inn}\left(1-W\right) + q'_{out}W \tag{3.52}$$

with

$$W\left(\eta\right) = \min\left(\frac{1}{2}\left\{1 + \frac{1}{\tanh\left(4\right)}\tanh\left[\frac{4\left(\eta - B\right)}{\left(1-2B\right)\eta + B}\right]\right\}, 1\right) \tag{3.53}$$

$$q'_{inn} = q'\left(\frac{y_{inl}}{R_\beta}\right) \tag{3.54}$$

$$q'_{out} = q'\left(y_{inl}R_\delta\right) \tag{3.55}$$

and

$$\eta = \frac{y_{inl}}{\delta_{inl}} \tag{3.56}$$

B denotes the location of the transition point from the inner and outer boundary layer and was set to 0.2. For this study the values $R_\beta = 0.987$, $R_\delta = 1.074$ and $\delta_{inl} = 2.065$ cm were used. The density in the inlet plane was calculated from temperature as follows:

$$\rho_{inl} = \rho_{inl}^{old}\frac{T_{inl}^{old}}{T_{inl}} \tag{3.57}$$

where the superscript *old* represents the value for those properties before the current recycling/rescaling step.

Chapter 4

Implementation

The runs investigated in this study were based on the crossing shock, turbulent boundary layer interaction at Mach 8.3 of Kussoy and Horstman [1]. The freestream conditions can be found in Table 4.1.

4.1 Geometry

Flat Plate

A flat plate solution was first done in order to develop the incoming boundary layer. The flat plate was 20 cm x 15.2 cm in the streamwise (X) and spanwise (Z) directions. The domain extends 20 cm in the normal (Y) direction. The grid for the coarse solution of the flat plate contained 81x145x61 points (691,200 cells). The fine grid solution doubled the number of points in the streamwise and spanwise directions, giving 161x145x121 points (2,764,800 cells). Points were evenly distributed in the streamwise direction and were progressively

Table 4.1: Experimental Conditions

	Description	Experimental Condition
M_∞	freestream Mach number	8.28
δ_∞(cm)	boundary layer thickness	3.25
δ^*_∞(cm)	displacement thickness	1.26
Re_{δ_∞}	Reynolds number	1.7×10^5
P_∞ (Pa)	freestream static pressure	430
T_w (K)	wall temperature	300
T_∞ (K)	freestream static temperature	80

clustered toward where the fins will be in the spanwise direction in preparation for later runs which will have fins just downstream of the flat plate. Cells were bunched toward the flat plate in the normal direction. The grid spacing in the wall-normal direction is constant throughout the domain.

Double Fin

The three-dimensional domain consisted of a 20 cm (in the flow direction) x 15.9 cm (in the transverse direction) flat plate (as explained in the previous section) followed by two perpendicular 10° fins (see Figure 4.1). There is also an outflow region past the throat which was 15 cm in the streamwise direction and 15.2 cm in the spanwise direction. The grid of the crossing shock calculation consisted of the same flat plate region was discussed previously in the inflow region (691,200 cells for the coarse grid solution and 2,764,800 cells for the fine grid case). Past the flat plate region, there were two 10° fins followed by a throat. The fins were 31 cm in the streamwise direction. The throat was 9 cm in the streamwise direction and approximately 4.27 cm in the spanwise direction. The throat and fin section grid was 81x145x121 points (1,382,400 cells) for the coarse grid and 161x145x241 points (5,529,600 cells) for the fine grid. The outflow region was discretized with 41x145x31 points (691,200 cells) for the coarse grid and 81x145x181 points (2,073,600 cells) for the fine grid. This makes for 2,764,800 cells in the coarse grid case and 10,368,000 cells for the fine grid case for the entire domain. An XZ cut of the coarse grid can be found in Fig. 4.2. The blocks for each processor are outlined in red. For the fine grid case, an equal number of points were used for each block, with four blocks for each of the coarse grid blocks.

4.2 Boundary Conditions

The walls of the domain had a no-slip boundary condition. There was also what has been termed a "isothermal ghost cell" [36] temperature boundary condition at the walls. Instead of setting the wall cell face to the wall temperature as with the standard isothermal wall condition, this condition imposed the wall temperature at the ghost cell:

$$T_{ghost} = T_{wall} \tag{4.1}$$

This allows the actual wall temperature to vary with applied heat loads. In the spanwise direction in the flat plate section, there was a periodic boundary condition. At the extreme of

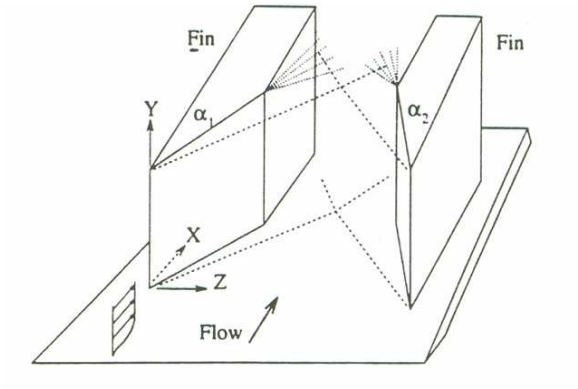

Figure 4.1: Double Fin Schematic

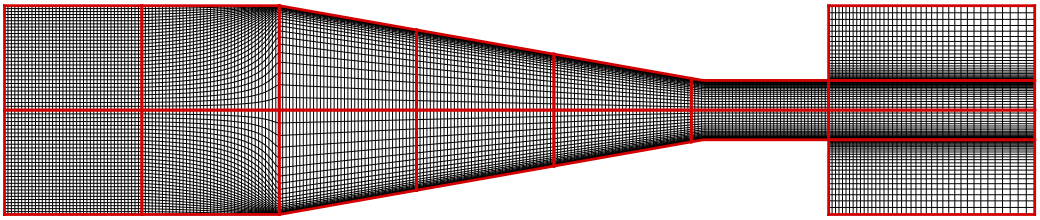

Figure 4.2: Coarse Mesh

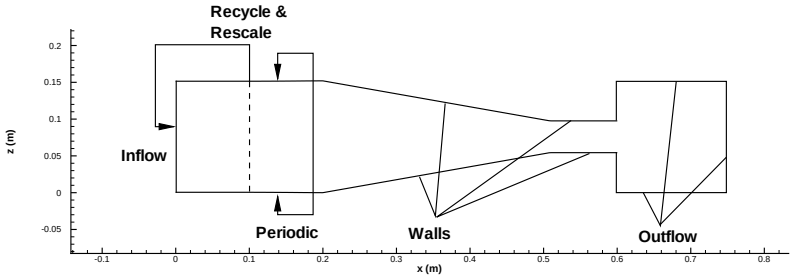

Figure 4.3: Boundary Conditions

the normal direction and the streamwise direction (at the outflow planes), there was a simple extrapolation boundary condition. The inflow condition depends on the recycling/rescaling procedure explained in Section 3.4. These conditions are shown in Fig. 4.3

4.3 Initialization

As mentioned earlier, LES/RANS flat plate solutions for both the fine and coarse grid cases were used to initialize the crossing shock interactions in the flat plate region. A RANS solution was performed for the entire interaction for the coarse grid in earlier work. [37] For the coarse grid case, the region downstream of the flat plate was initialized with the RANS solution. For the fine grid case, the region downstream of the flat plate was initialized using an interpolated solution from the completed coarse grid LES/RANS hybrid solution. The simulation was allowed to run until the heat transfer levels sufficiently stabilized at the wall. Once this had occurred, statistical data was collected. For the RANS cases, the inflow plane was set to a RANS solution.

Chapter 5

Results and Discussion

5.1 Flat Plate Results

Before running the entire crossing-shock simulation, the flat-plate section of the experiment was simulated. This step was necessary to validate the recycling/rescaling procedure and its ability to develop and maintain a realistic boundary layer. As mentioned earlier, periodic boundary conditions were used in the transverse direction. Extrapolated boundary conditions were used in the outflow plane and in the positive y direction. No-slip and isothermal ghost cell conditions (as explained in Sec. 4.2) were used for the flat plate. A recycling/rescaling procedure was used for the inflow plane. An in-depth study of the flat-plate results can be found in Ref. [37]. From this source it was found that the LES to RANS transition factor A should be set to 25 (which leads to a predicted transition point of $d^+ = 225$) for best agreement with the data of Kussoy and Horstman [1].

This study showed similar trends. Experimental profiles were measured 3 cm upstream of the vertical fins. The computational results from this location are compared to the experimental values to validate the simulation before any shock interactions occur. The results were time-averaged for the cases using the unsteady hybrid model. Statistics were gathered for 18.6ms of physical time for the BSL case and 14.0ms of physical time for the SST case. Unless otherwise noted, all the cases shown in this section are for the fine grid case, with either a RANS turbulence model or our hybrid LES/RANS model.

The velocity and transformed velocity profiles, seen in Figs. 5.1 and 5.2, predicted by the hybrid models show good agreement with experimental data. The predicted Mach number profiles in Fig. 5.3 all fall below the experimental values. This is likely due to the

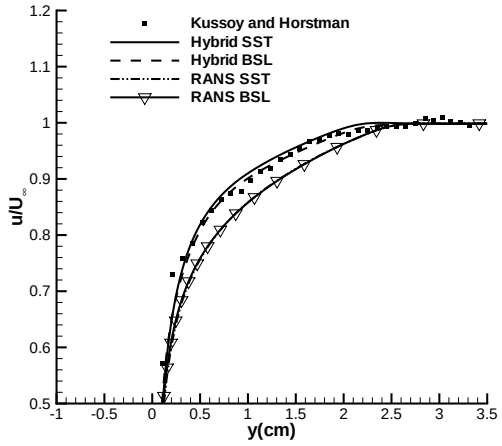

Figure 5.1: Flat plate velocity profile

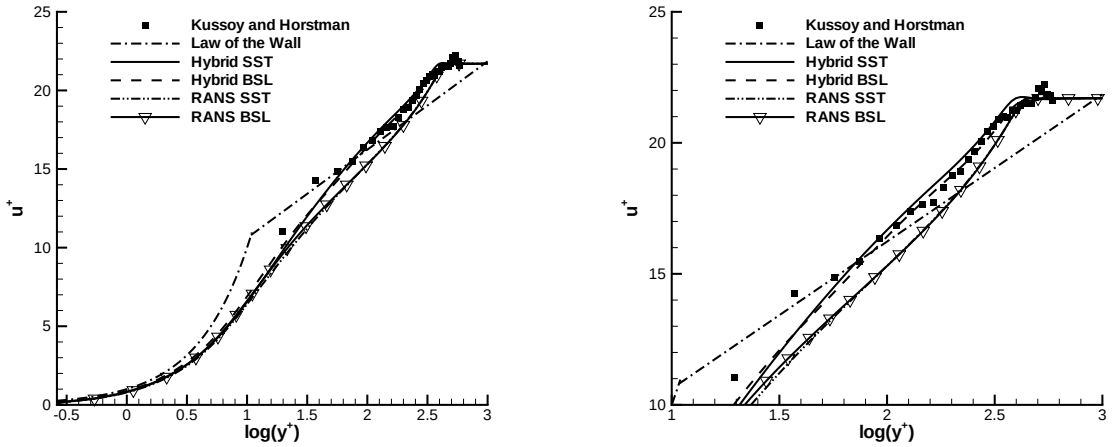

(a) Full Profile

(b) Detail

Figure 5.2: Van Driest-transformed velocity profile in flat plate region

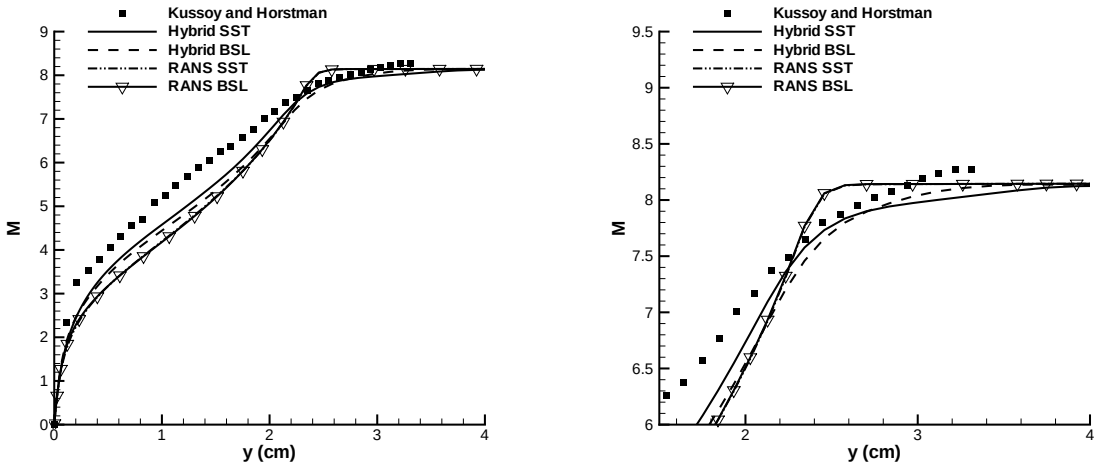

(a) Full Profile

(b) Detail

Figure 5.3: Mach number profile in the flat plate region

Table 5.1: Heat transfer 3.0 cm upstream of fins

Case	Heat Transfer (W/cm^2)
Experiment	10400
Hybrid SST	11200
Hybrid BSL	14349
RANS SST	12647
RANS BSL	13187

over-prediction of the temperature by all models tested, as can be seen in Fig. 5.4. And, since the hybrid SST model best-predicted the temperature profile, it is also best-predicts the Mach number profile. Table 5.1 shows the wall heat transfer three centimeters upstream of the fins. As the temperature profile would suggest, the predicted heat transfer at the wall is higher than the experimental heat transfer for all the cases. As with the temperature profile, the hybrid SST heat transfer prediction was the closest to the experimental data. This correlation does not hold for all the cases though – the hybrid BSL model with the highest predicted heat transfer rates at $x = -3.0\,cm$ would be expected to have the highest temperature profile as well. Instead, both of the RANS cases have the higher temperature profile prediction than the hybrid BSL case.

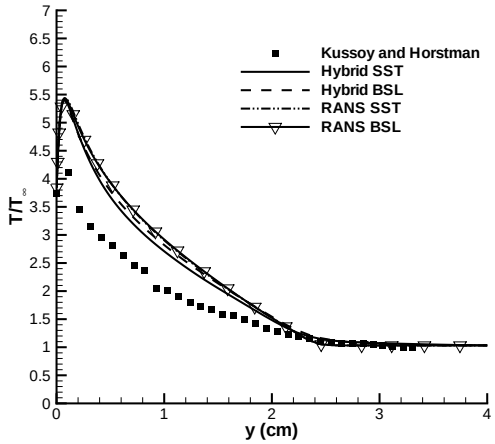

Figure 5.4: Temperature profile in flat plate region

Figure 5.1 shows that the size of the velocity boundary layer was well-predicted in all cases. A detail of the transformed velocity boundary layer can be found in Fig. 5.2(b). It was not entirely clear whether the thermal boundary layer was correctly sized between the four different runs. Fortunately a detail of the Mach profile (5.3(b)) can provide some insight. The RANS cases slightly underpredicted the size of the Mach boundary layer. Since the velocity profile was predicted correctly by the RANS models, it can be assumed that that the RANS models incorrectly modeled the size of the thermal boundary layer.

The laminar viscosity profiles in Fig. 5.5 showed similar trends for all models. The turbulent viscosity profiles (Fig. 5.6) on the other hand show major differences between the hybrid and RANS predictions. As expected, the turbulent eddy viscosity for the hybrid models was far smaller than predicted with RANS. Also of note is the decrease in eddy viscosity due to the SST modification to the Menter model for the hybrid cases. This phenomenon was noted in the development of the Menter model [12]. A plot of the resolved and modeled TKE profiles is shown in Fig. 5.7. The hybrid SST model showed higher resolved TKE (in green) and lower modeled TKE (in red) than the BSL model. The SST modification also increased the TKE of the RANS model slightly. Resolved TKE is calculated as follows:

$$k_{resolved} = \frac{1}{2\overline{\rho}}\left(\overline{\rho u^2} + \overline{\rho v^2} + \overline{\rho w^2} - \frac{\overline{\rho u}}{\overline{\rho}} - \frac{\overline{\rho v}}{\overline{\rho}} - \frac{\overline{\rho w}}{\overline{\rho}}\right) \tag{5.1}$$

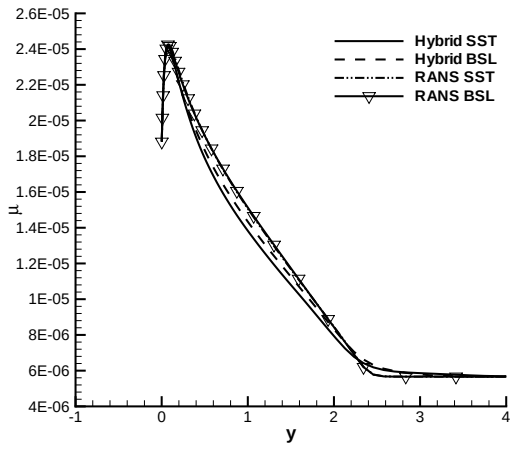

Figure 5.5: Laminar viscosity profile in flat plate region

The modeled TKE predictions for both hybrid models are lower than the RANS prediction. The blending function is also shown, and the transition point to the LES model is slightly below y=1.0 cm. By this point, the resolved TKE for both hybrid models are quite close and slightly higher than the pure RANS TKE.

Contours for TKE can be seen for the four different models in Fig. 5.8. Curiously, the time-averaged TKE contours for the hybrid cases displayed asymmetry and streak-like patterns when they should have been homogeneous in the transverse direction, if sufficiently statistically converged. The hybrid BSL case showed less extreme changes in the transverse direction, but was still not homogeneous. This behavior suggests that the vortical structures that are characteristic of unsteady LES flows (which can be seen in Fig. 5.9) kept the same basic structure and position throughout the simulation. It would be expected for the flow to be more randomized and thus, the time-averaged data in the flat plate would be effectively uniform in the spanwise direction. This problem could be attributed to the recycling/rescaling procedure used in the simulation. The placement of the recycling plane 10 cm from the inflow boundary may not give the flow enough time to change significantly from its inflow state before it is recycled. The recycle plane was located at x=10.0cm. It can be seen in Fig. 5.10 that there is periodicity in the temperature contour. The period was approximately 10 cm in the streamwise direction. Animated contours of temperature show that these periodic contours do not move much in the transverse direction. Differences

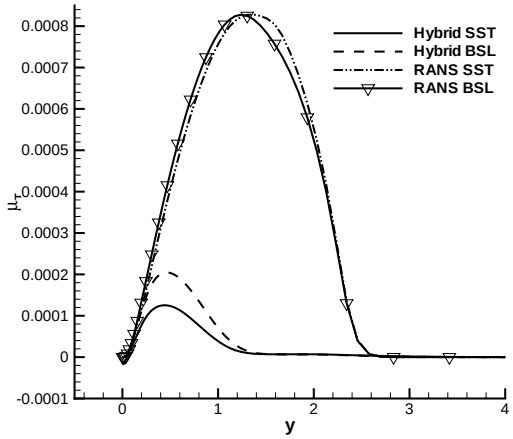

Figure 5.6: Turbulent viscosity profile in flat plate region

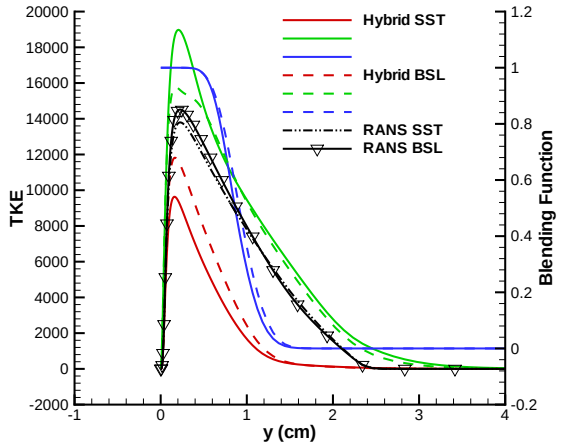

Figure 5.7: Turbulent kinetic energy profiles and blending function in the flat plate region (for the hybrid cases red indicates modeled TKE, green indicates resolved TKE, and blue indicates blending function)

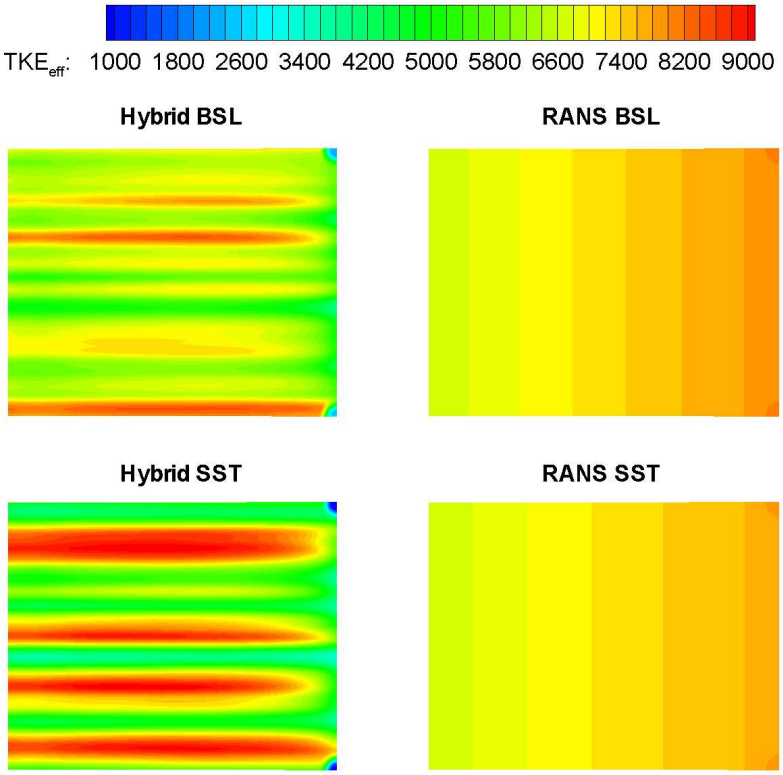

Figure 5.8: Time-averaged turbulent kinetic energy (TKE) at $y = 1.0cm$ upstream of the fins

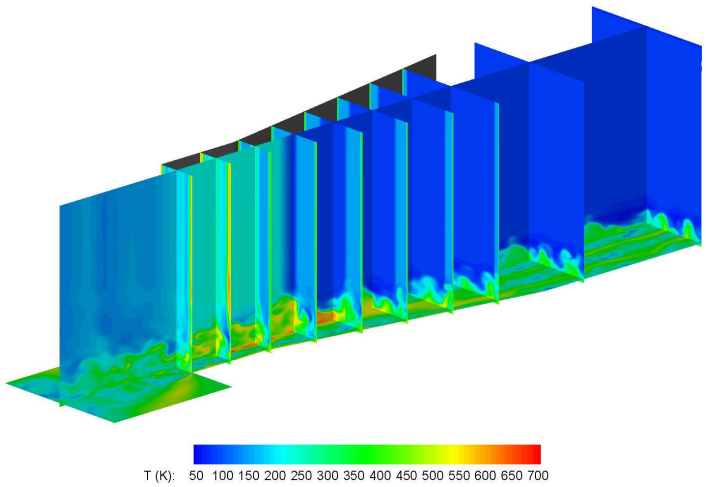

Figure 5.9: Instantaneous 3-D temperature contour, hybrid SST case

in the transverse homogeneity could also be attributed to the fact that the hybrid SST case was run for less physical time than the hybrid BSL case.

5.2 Crossing Shock Results

First, to get an idea of the flow structure of the interaction, two-dimensional slices of the temperature contour along the XY center plane, the bottom surface ($y = 0.0038m$) and numerous XZ planes along the length of the domain are shown in Fig. 5.9. The boundary layer separation due to the crossing shock interaction is evident. The oblique shocks are evident as they approach the center from the leading edges of the double fins Also vortical structures along the centerline toward the bottom wall are present. There is also evidence of high heating loads in the vicinity of the crossing shock interaction. The heat transfer in this region is of particular importance for the design of hypersonic inlets.

When viewing just the center plane (Fig. 5.10) the shock front itself is clearly visible just aft of the boundary layer separation. The turbulent boundary layer growth is also more visible in this view. The boundary layer is clearly growing along the length of the flat plate. Also of note is the very periodic nature of the boundary layer. Ideally a boundary layer with a more random structure would be modeled. Unfortunately this periodicity is at least partially a consequence of the recycling procedure detailed in the previous section.

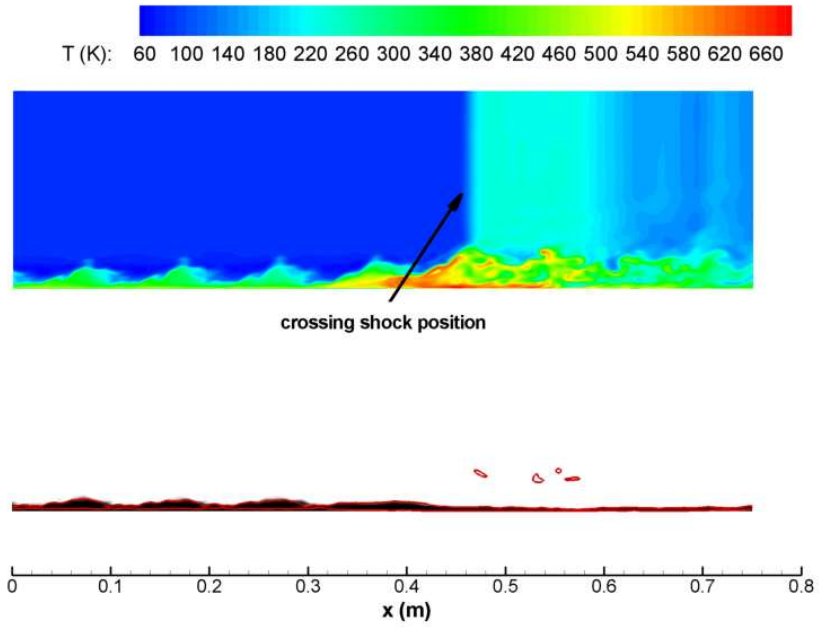

Figure 5.10: Instantaneous temperature and blending function contours (dark for RANS, light for LES) in the XY plane – the red contour indicates $\mu_t/\mu_\infty = 20$

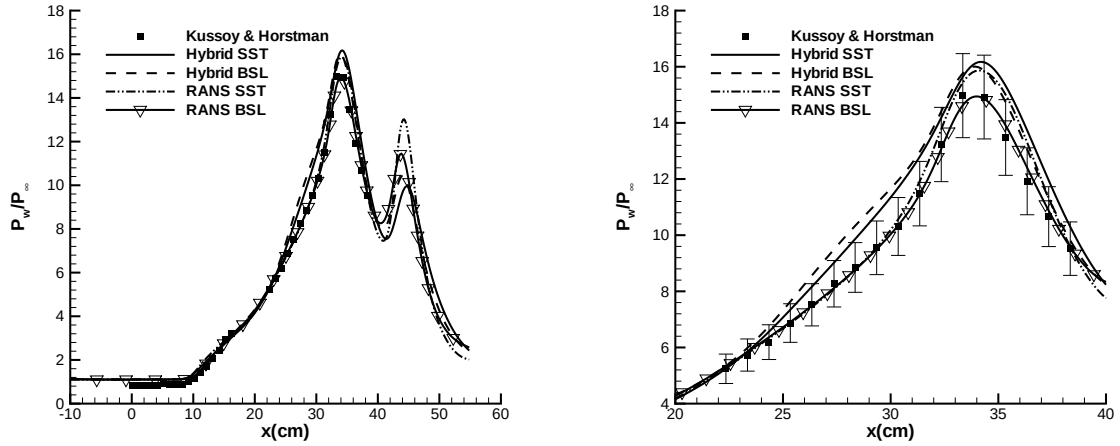

(a) Complete interaction

(b) Detail

Figure 5.11: Centerline pressure

The blending function is shown just beneath the temperature contour to show its dynamic nature. A contour for $\mu_t/\mu_\infty = 20$ is shown in red on the same plot as the blending function. As expected, the blending function correlates nearly exactly with the eddy viscosity. After the separation of the boundary layer, the flow was modeled almost entirely by the LES model.

For comparison to experimental values, time averaging was required. Unlike the flat plate results, data for the complete interaction could not be averaged in the transverse direction due to the three dimensional nature of the interaction. This time averaging required much longer computational runs for statistical convergence. Both Menter SST and Menter BSL results are shown for the RANS and hybrid cases. The centerline wall pressure profile (Fig. 5.11) showed good agreement with experimental data for all cases attempted. The error bars shown for surface pressure were given by Kussoy and Horstman [1] to be $\pm 10\%$ or $\pm 80 N/m^2$, whichever is greater. The RANS SST case shows the best agreement with experimental data, with the RANS BSL case also showing good agreement. The hybrid cases only fell outside the experimental margin of error at about half the stations, though its prediction is not as good as the RANS cases. The hybrid cases tended to overpredict the pressure profile while the RANS BSL case tended to underpredict it.

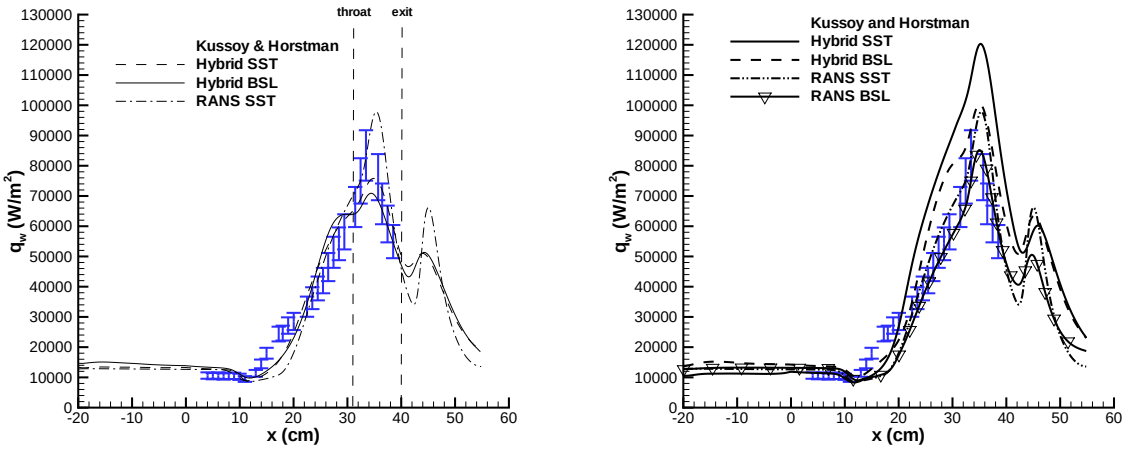

(a) Coarse Grid

(b) Fine Grid

Figure 5.12: Centerline heat transfer, experimental error bars in blue

The centerline heat transfer results were not nearly as consistent with the experimental data. The coarse grid results for the hybrid cases looked promising, with a profile that improved upon the RANS case and fell within the experimental error ($\pm 10\%$) for nearly every point (Fig. 5.12(a)). The refinement of the grid yielded higher heat transfer for the hybrid cases (Fig. 5.12(b)). As can be seen in Fig. 5.13, the instantaneous heat transfer values for the hybrid cases are smilar to those predicted for the RANS cases. The time averaging though, showed reduced off-center values for the hybrid cases. The centerline heat transfer was increased, however, as the hotter off-center fluid was transported toward the center due to the unsteadiness of the flow. A characteristic of the SST modification to the Menter model is the reduction of eddy viscosity and the turbulence length scale. This reduced eddy viscosity allowed for less damping of the temperature fluctuations and more movement of the hotter off-center fluid toward the centerline. This was likely the root of the increased heat transfer for the SST cases over BSL cases. This modification did not seem to affect the flow adversely in the flat plate region, though in the converging section the heat transfer is more severe.

The RANS models did a good job in predicting the centerline properties, but when comparing the predicted pressure and heat transfer data in the transverse direction with

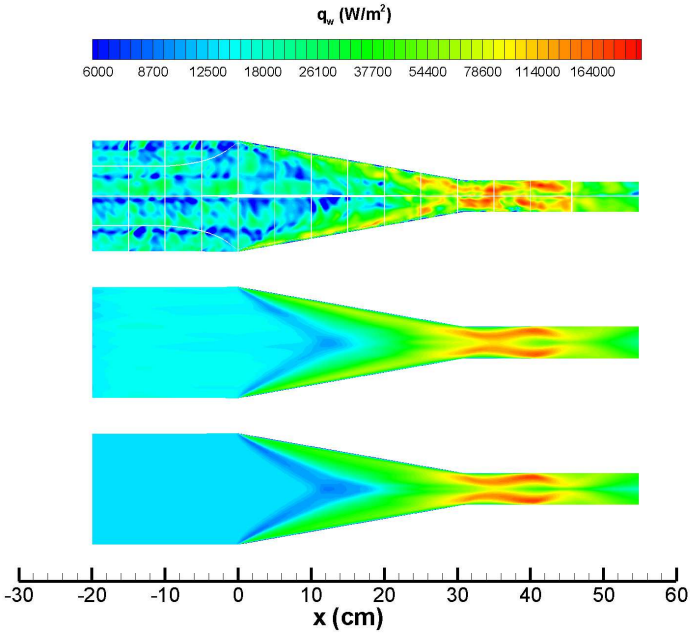

(a) BSL

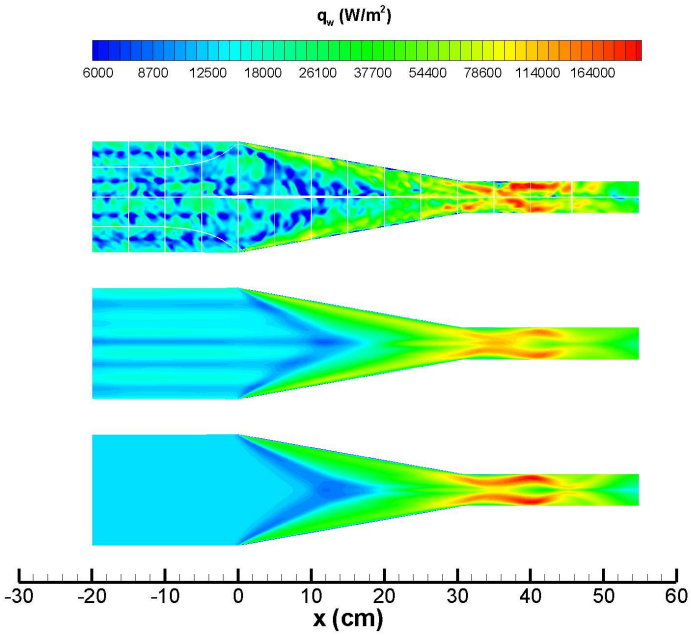

(b) SST

Figure 5.13: Wall heat transfer contours, top - instantaneous contours for hybrid models, middle - time-averaged contours for hybrid models, bottom - RANS contours

experimental measurements, there was not much success with any model. The transverse pressure plots show a reasonable agreement with experimental data with exception of the last station. The first station shows good agreement with experimental data for all models. The RANS models predicted the transverse pressure at the second station well and the hybrid models overpredicted the peak in pressure at the centerline (as can also be seen in Fig. 5.11). Only the RANS BSL case was able to capture the transverse pressure profile for the third station, while the rest overpredicted the pressure in the centerline region.

Experimental flow-field pitot pressure data was provided by Kussoy and Horstman [1]. Contour plots for all four fine grid cases follow (with identical contour levels for comparative purposes). Station 1 (Fig. 5.16) is situated 18.0 cm aft of the double fin leading edge and is upstream of the oblique-shock crossing position. This is evident by sharp pressure gradients in the transverse direction above y = 4.0 cm. All of the models capture the shock position well. The differences among the pitot pressure contours appear more in the structure of the flow closer to the body. The hybrid SST case clearly shows evidence of multiple vortical structures. It is also notable that the hybrid SST solution is slightly asymmetric; running the case further would have resulted in a more symmetric solution. This asymmetry may also be tied to the lack of randomization upstream in the flat plate section as discussed in the previous section. At Station 2 the RANS cases exhibit more extreme variations in pitot pressure. Upon examination of the static pressure contours, no significant differences between the schemes could be found. The calculation of pitot pressure used is as follows for supersonic flow (for locally subsonic flow, the stagnation pressure is used):

$$P_{T2} = P_1 \frac{\gamma+1}{2} M_1^2 \left(\frac{\frac{\gamma+1}{2} M_1^2}{\frac{2\gamma}{\gamma+1} M_1^2 - \frac{\gamma-1}{\gamma+1}} \right)^{\frac{1}{\gamma-1}} \tag{5.2}$$

Since the pitot pressure is only dependent on static pressure and Mach number, the Mach number contours are also compared at station 2 (Fig. 5.20). The RANS cases show lower Mach numbers for the majority of the flow below y = 4.0 cm, which would explain the lower minimum pitot pressures for the RANS case. This, however, does not explain the higher peak pitot pressure for the RANS cases. This phenomenon can be explained by the low pressure which comes higher off the wall for the hybrid case than the RANS cases. The reduction of extrema in the hybrid cases was due to the unsteadiness of the method and the fact that the data shown was time-averaged. The extrema in pitot pressure oscillated with the flow in the unsteady hybrid cases, thus with time averaging of flow properties,

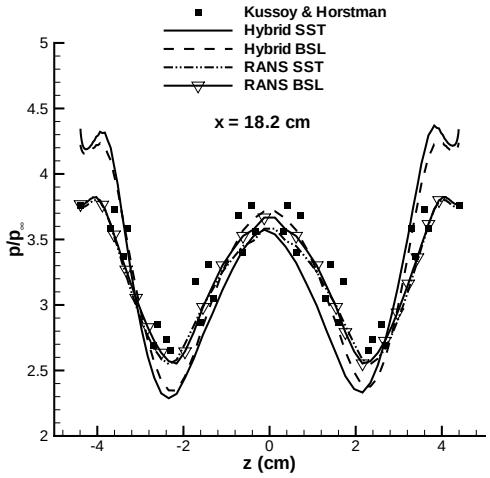

(a) Station 1

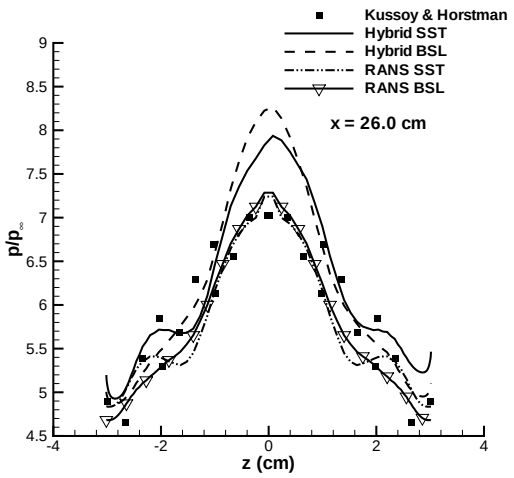

(b) Station 2

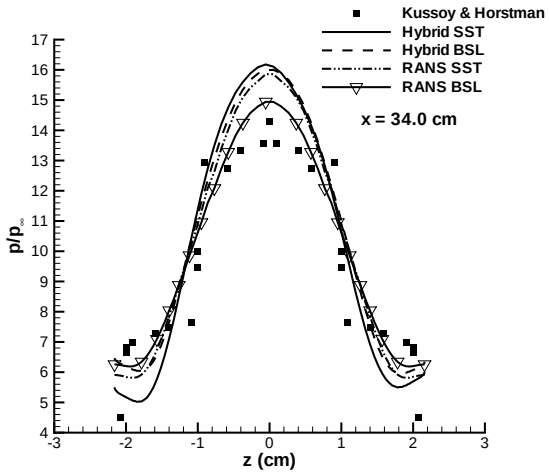

(c) Station 3

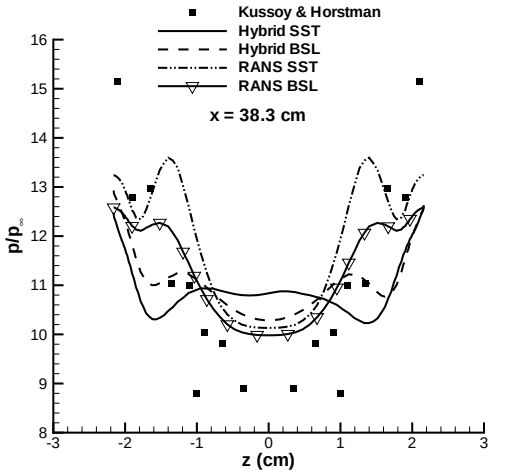

(d) Station 4

Figure 5.14: Transverse surface pressure, fine grid

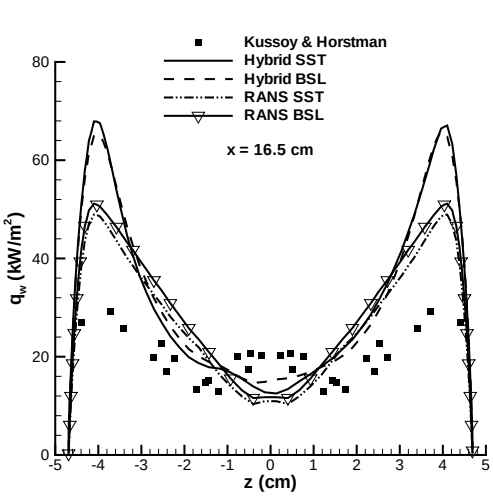

(a) Station 1

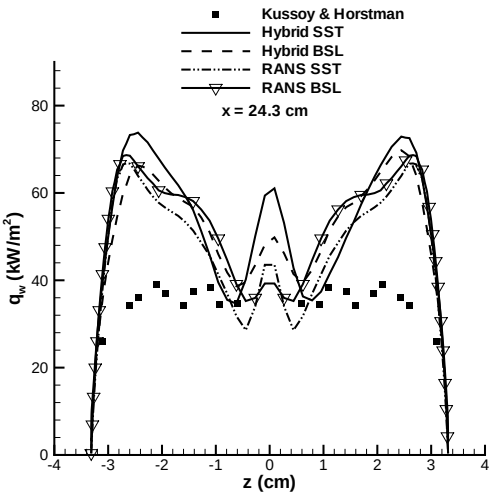

(b) Station 2

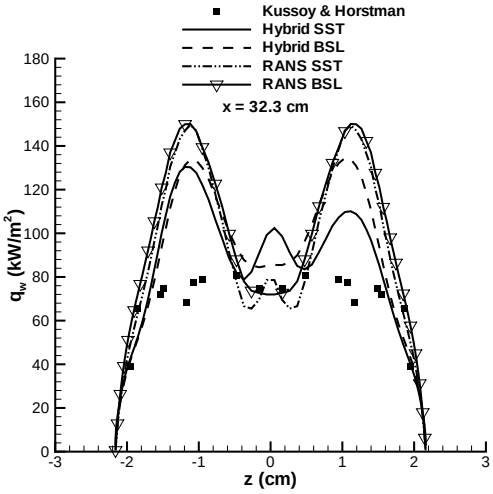

(c) Station 3

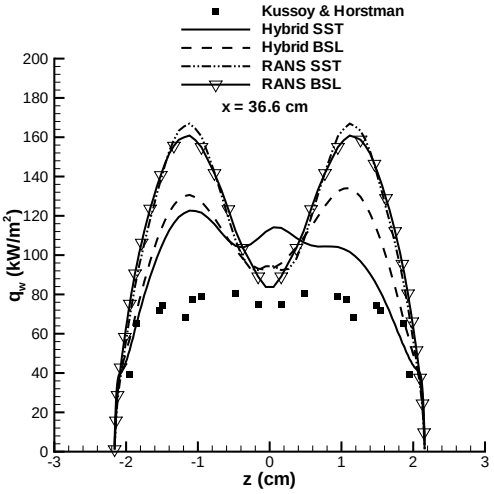

(d) Station 4

Figure 5.15: Transverse wall heat transfer, fine grid

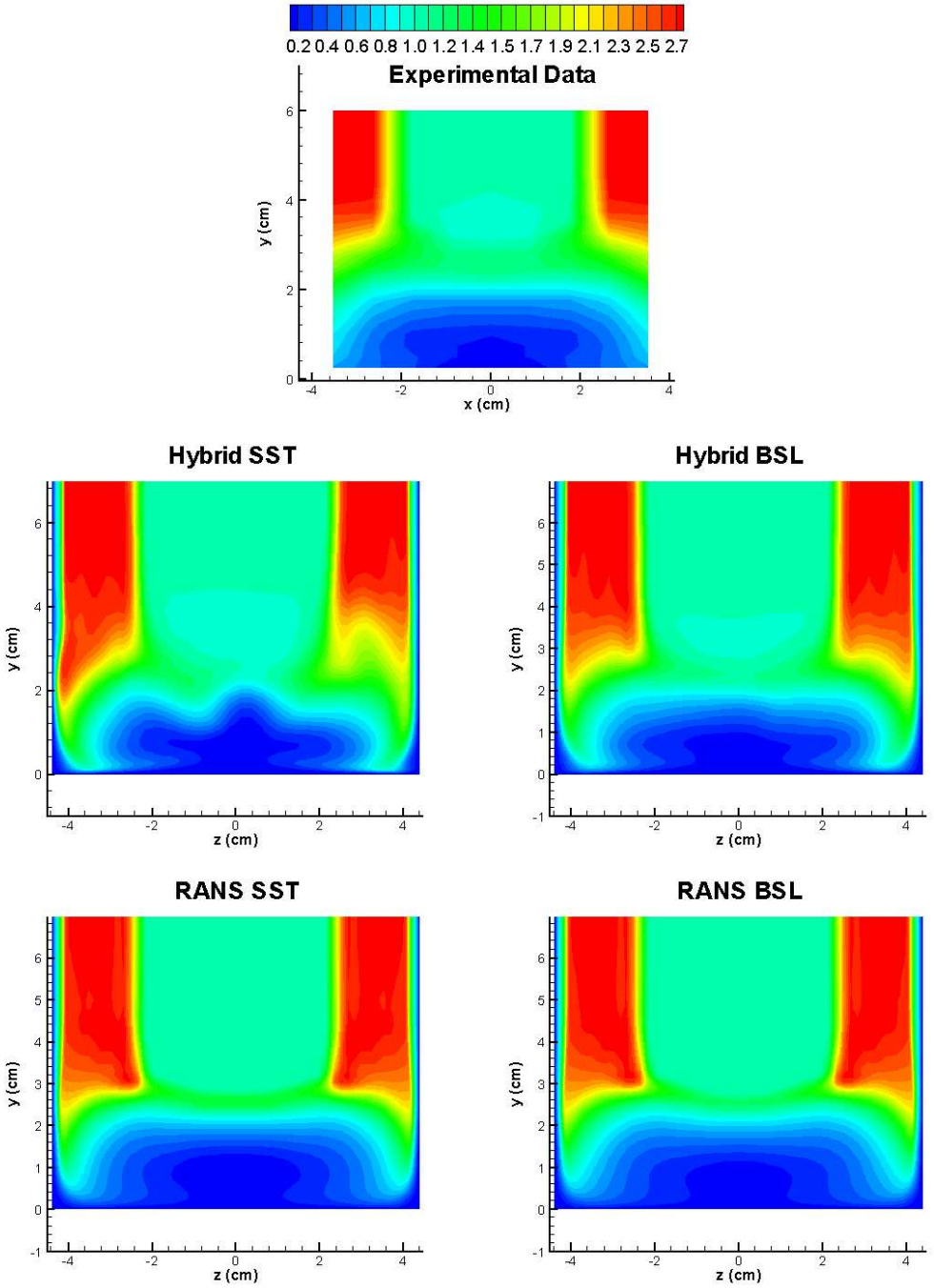

Figure 5.16: Pitot pressure contours ($P_T/P_{T,\infty}$) at station 1 (x = 18.2 cm)

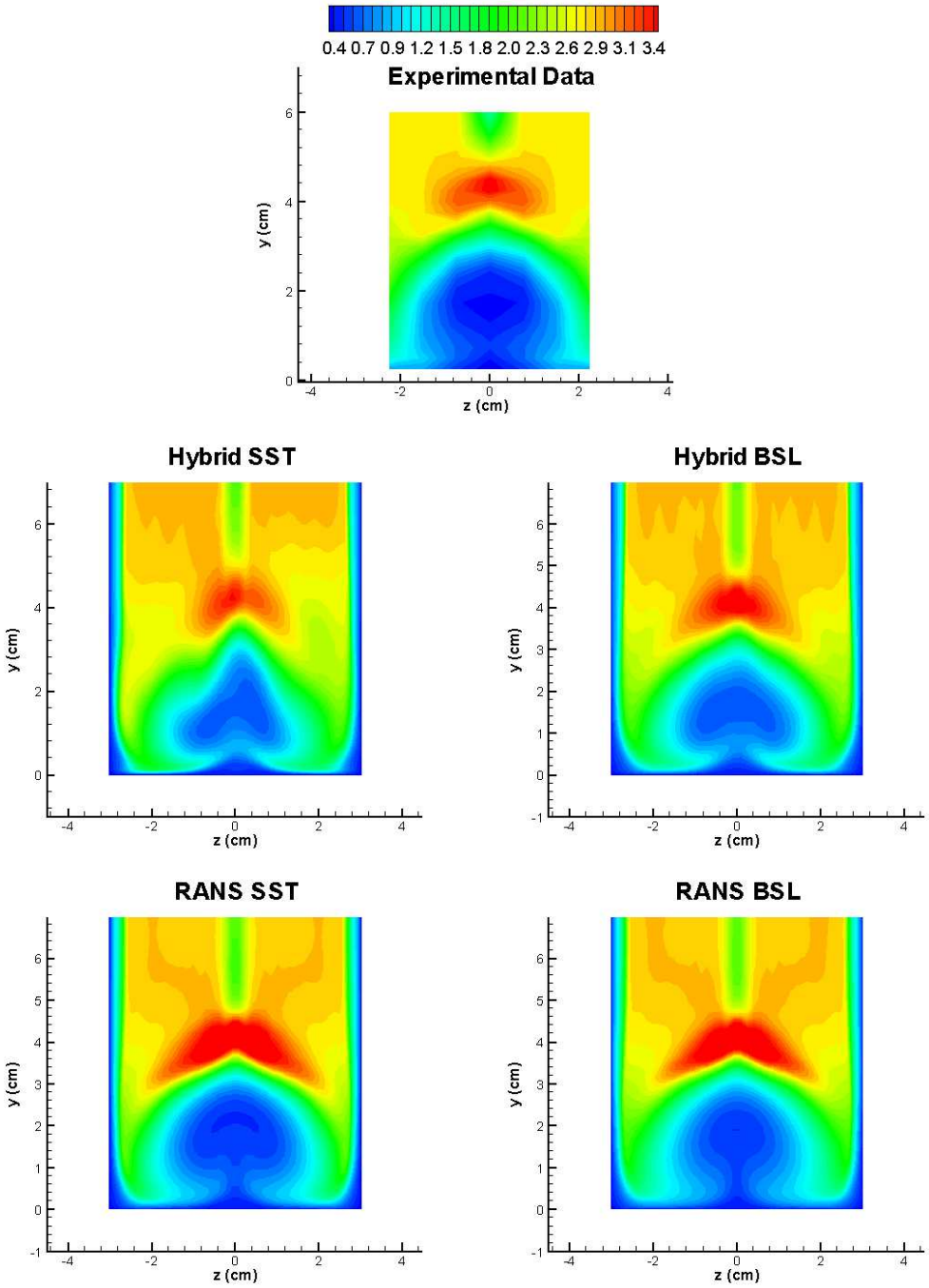

Figure 5.17: Pitot pressure contours ($P_T/P_{T,\infty}$) at station 2 (x = 26.0 cm)

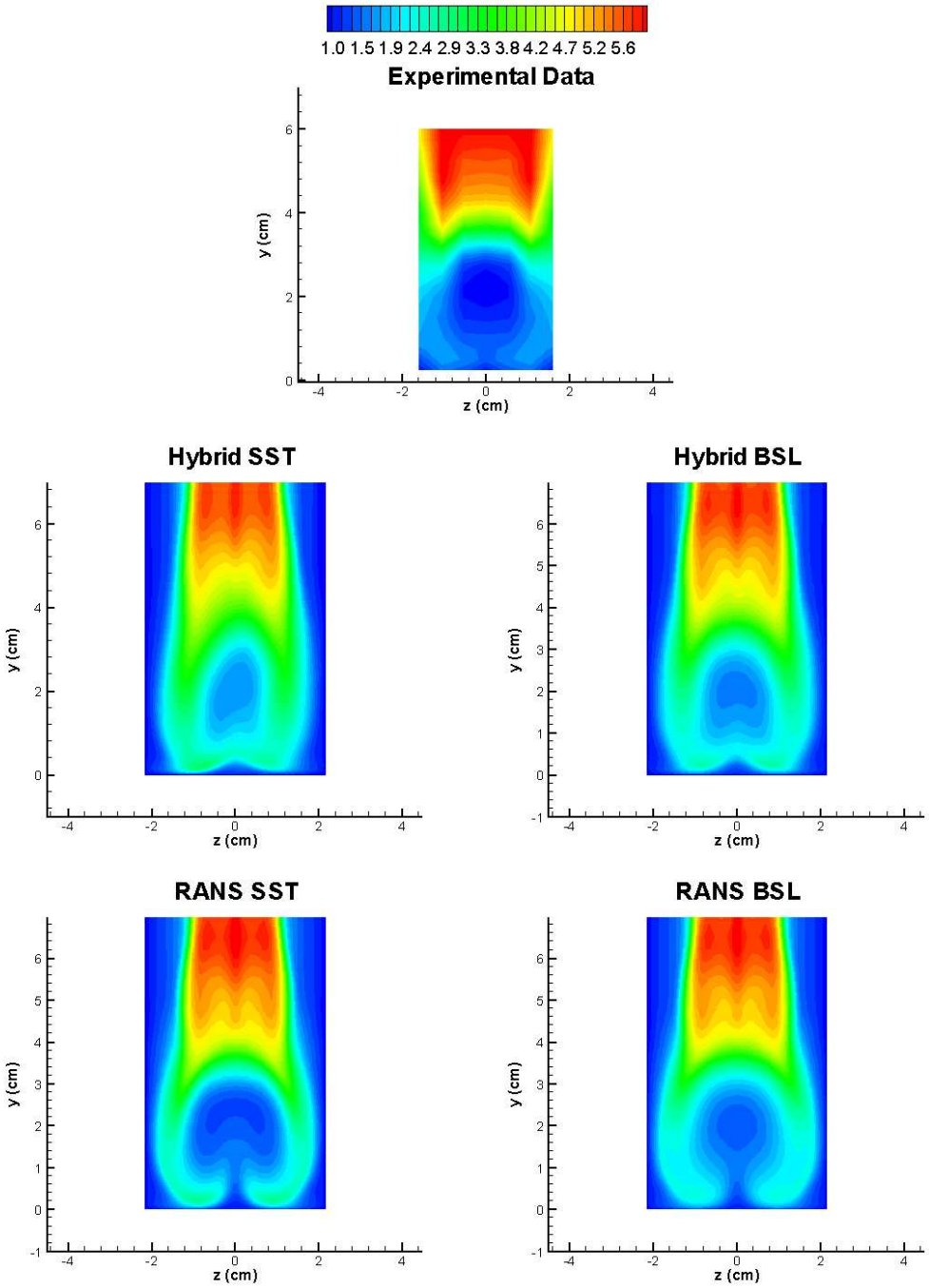

Figure 5.18: Pitot pressure contours ($P_T/P_{T,\infty}$) at station 3 (x = 34.0 cm)

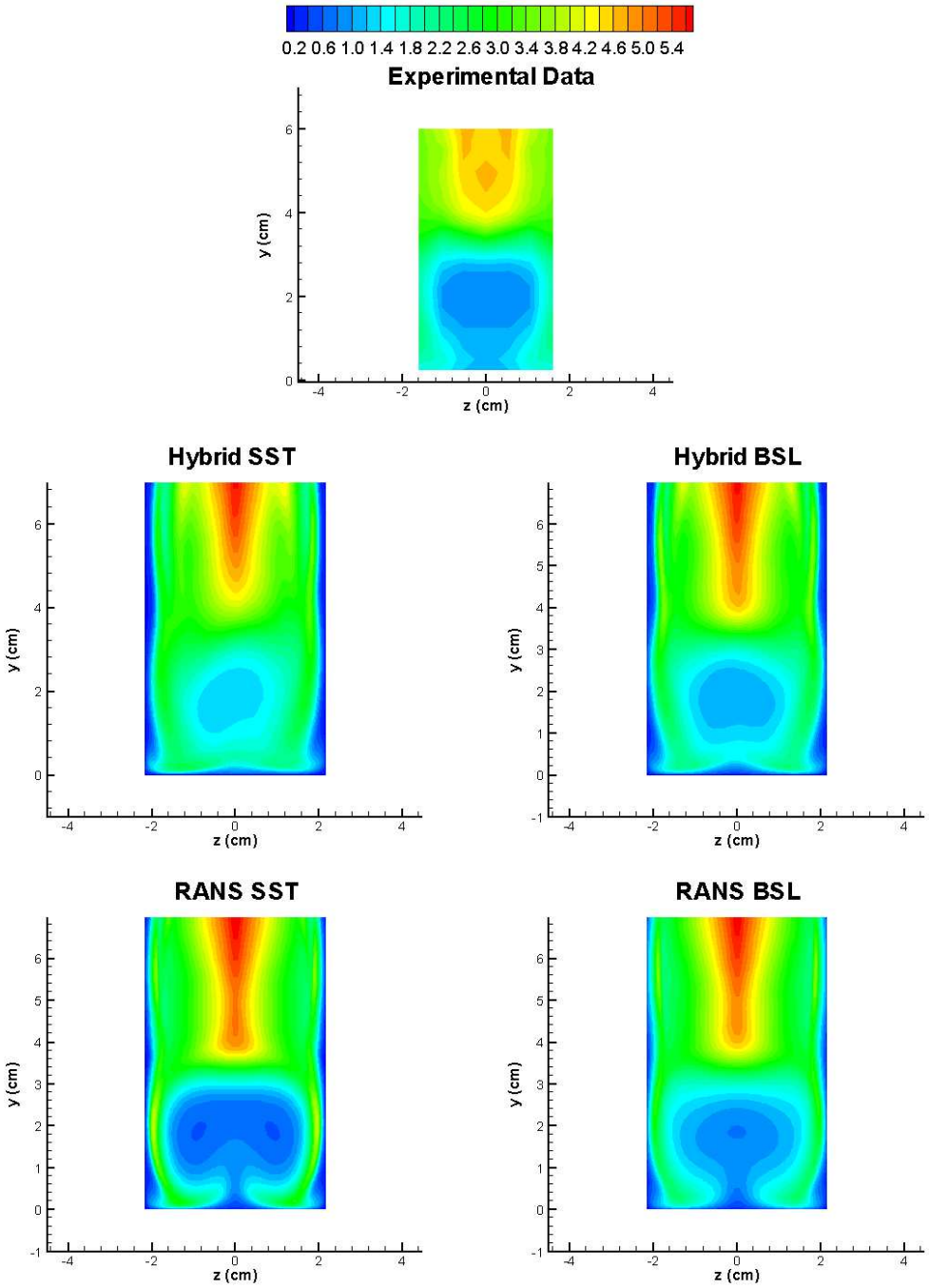

Figure 5.19: Pitot pressure contours ($P_T/P_{T,\infty}$) at station 4 (x = 38.3 cm)

these extrema were smeared over a larger area. The difference between the pitot pressure contours for the hybrid and RANS cases could also be due to the fact that pitot pressure itself was not time-averaged for the hybrid cases, but instead was calculated from time-averaged Mach number and static pressure. This same phenomenon can be observed in Figs. 5.18 and 5.19.

In order to better understand the structure of the vortical structures formed by the shockwave boundary layer interaction, contours for helicity for each run are shown in Figs. 5.21-5.24. Vortices in this crossing shock interaction act to bring higher energy flow down to the wall, resulting in higher heat fluxes at the wall. Helicity is defined as the dot product of velocity and vorticity. It is effectively the degree to which the fluid moves in a helical path, with the sign indicating whether the helix is rotating clockwise or counterclockwise. The contour lines indicate constant lines of helicity ($\pm 1 \times 10^6 m^2/s^2$, $\pm 2 \times 10^6 m^2/s^2$ and $\pm 5 \times 10^6 m^2/s^2$). The range for the flood contours is more narrow (between $-1 \times 10^5 m^2/s^2$ and $1 \times 10^5 m^2/s^2$) so that the locations of weaker vortices are visible. Figure 5.21 shows that both hybrid models are asymmetric about the centerline. There are two main counter-rotating vortices at every station with smaller (normally less intense) counter-rotating vortices surrounding the main large vortices. The contour lines at station 1 show that the hybrid models have a large intense section of the main vortices with the hybrid SST model showing the largest area with helicity above $5 \times 10^6 m^2/s^2$ and the RANS BSL model having the weakest. This trend of the hybrid models and the SST modification increasing the intensity of the main vortices holds for the second station as well. Other than very weak and narrow vortices present above the main vortices for the RANS models, the overall structure of the vortices is similar among all models. The main center vortices lose much of their strength by station 3 and 4 while the wall vortices gain strength. The RANS SST predictor shows small vortices above the main center vortices at station 3. By station 4 all the models show these two counter-rotating vortices above the main vortices, though they are by far the largest in the RANS SST case and are barely visible in the hybrid SST case. The side-wall vortices weaken substantially at station 4 as well. The vortices on the bottom wall are stronger at station 4 for the hybrid models; this could be reason for the higher centerline heat transfer for these models.

The multiple vortical structures can be observed in the turbulent kinetic energy contours as well (see Figs. 5.25 - 5.28). The TKE contours show major differences between the RANS and hybrid models in their predictions of the vortical structures and the flow

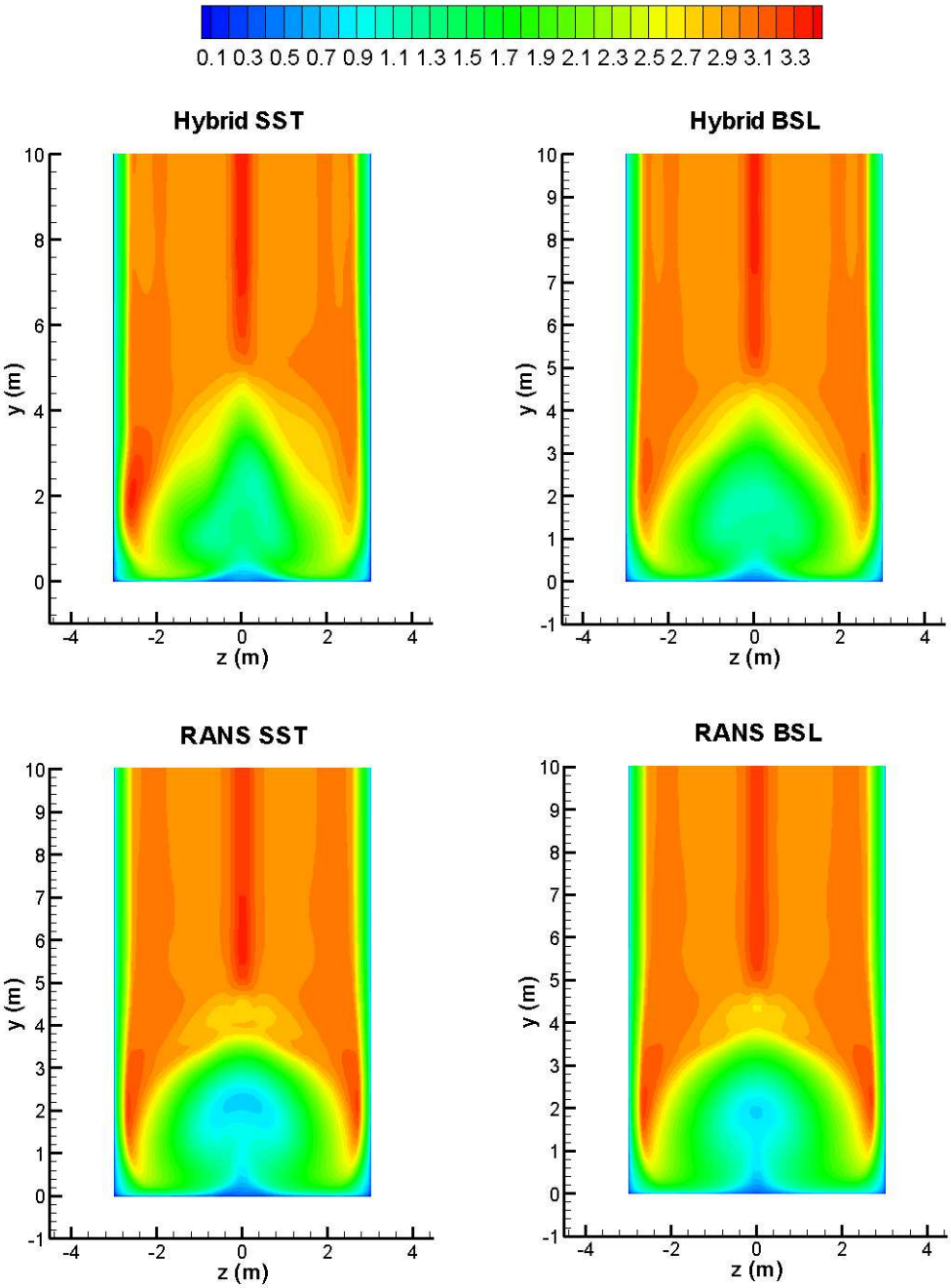

Figure 5.20: Mach contours at station 2, x = 26.0 cm

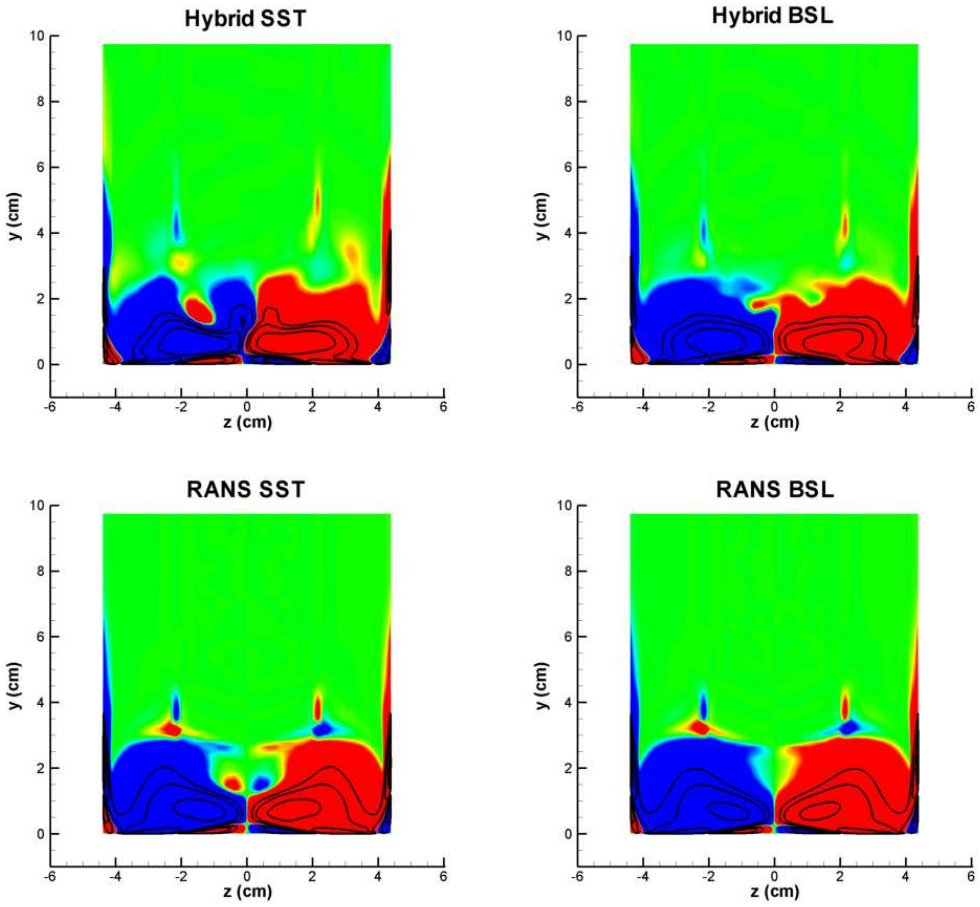

Figure 5.21: Helicity contours at station 1, x = 18.2 cm

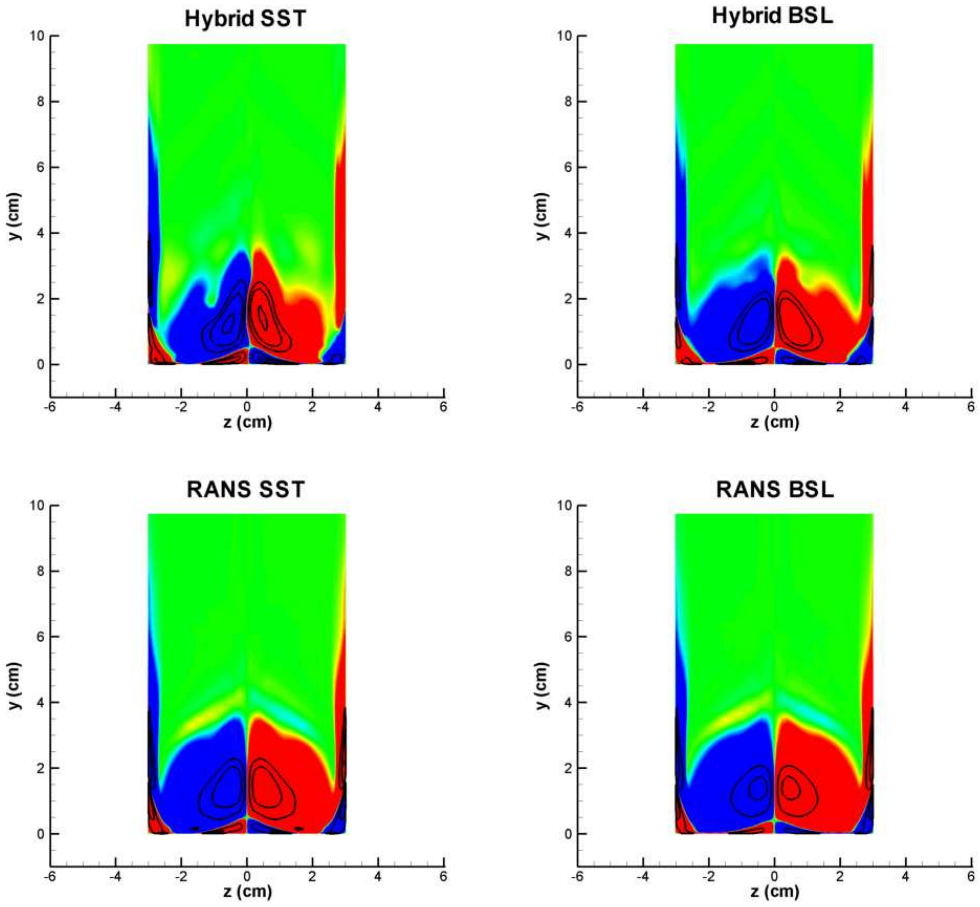

Figure 5.22: Helicity contours at station 2, x = 26.0 cm

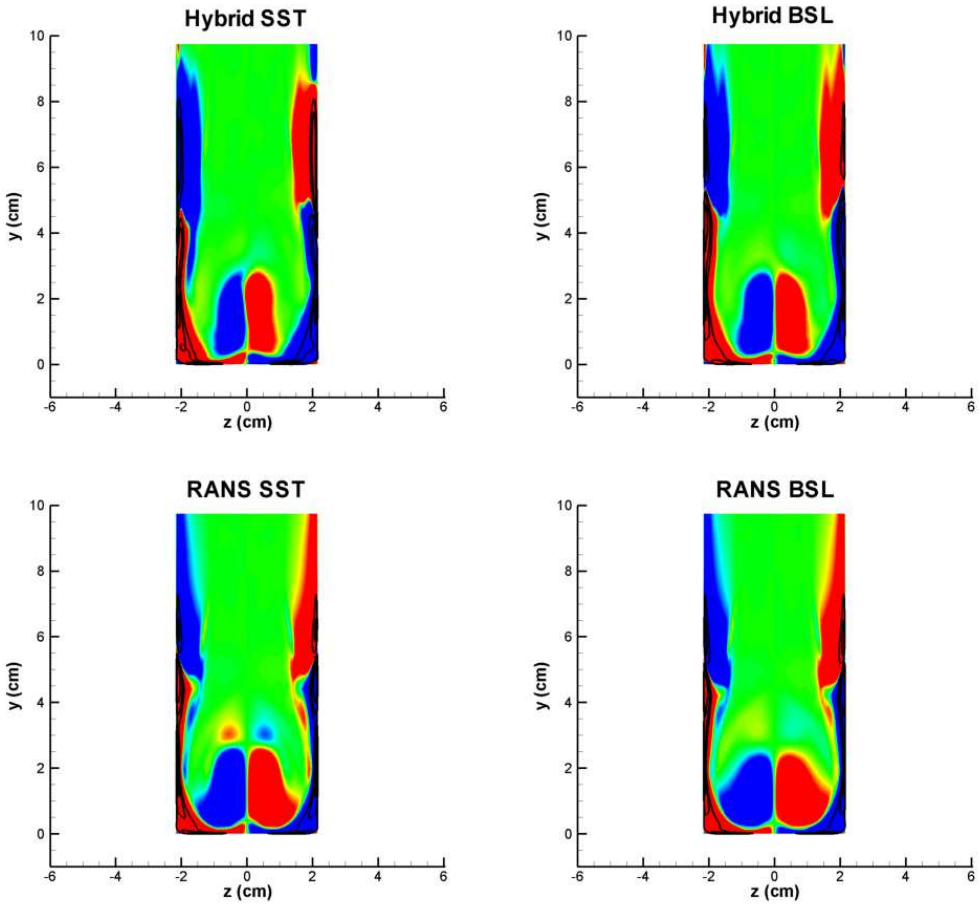

Figure 5.23: Helicity contours at station 3, x = 34.0 cm

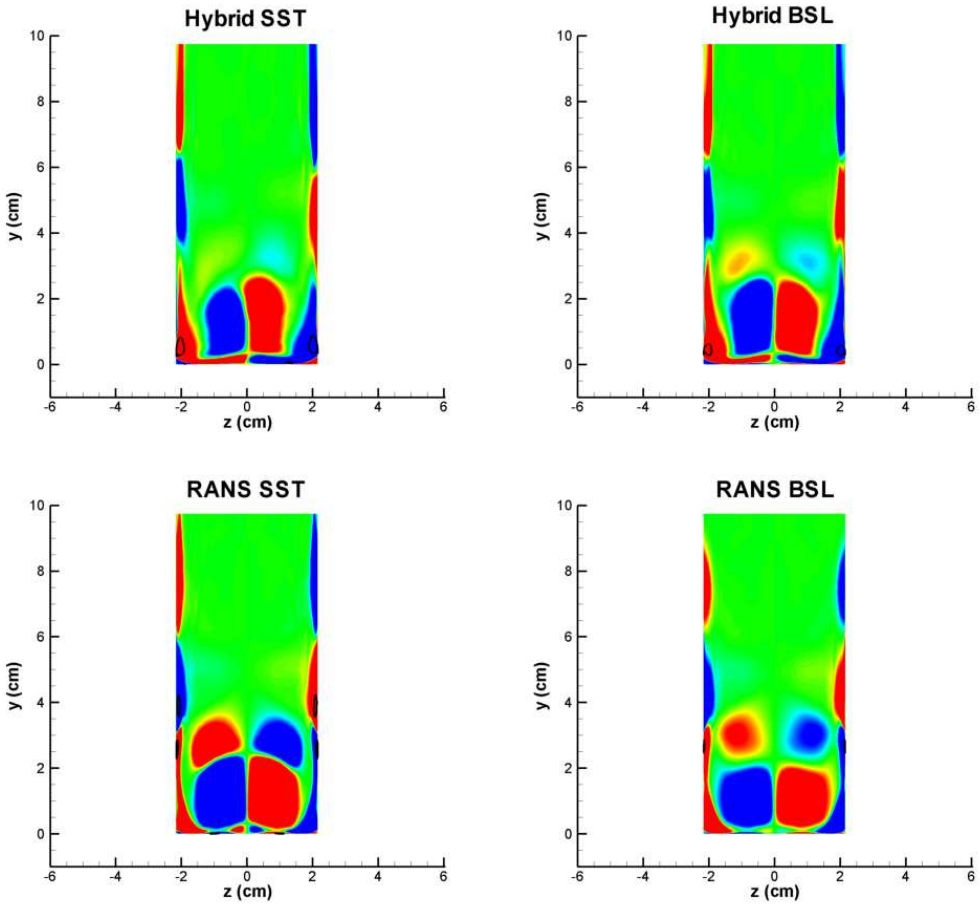

Figure 5.24: Helicity contours at station 4, x = 38.3 cm

near the body. The most notable differences are at stations 3 and 4. At these stations, the hybrid models predict vortical structures that are stronger close to the bottom wall than the RANS cases. This difference could provide a further explanation of the higher wall heat transfer for the hybrid models. The predictions for the side wall TKE look similar for all models with the exception of station 4. At this last station, there is a high heat transfer load on the side walls centered around y = 4 cm for the hybrid SST model. This load does not correspond to a strong side wall vortex at this location (see Fig. 5.24). In fact, the RANS SST case shows the strongest side wall vortices near that location and has far lower heating loads than the hybrid SST model. The cause of this heating is not clear.

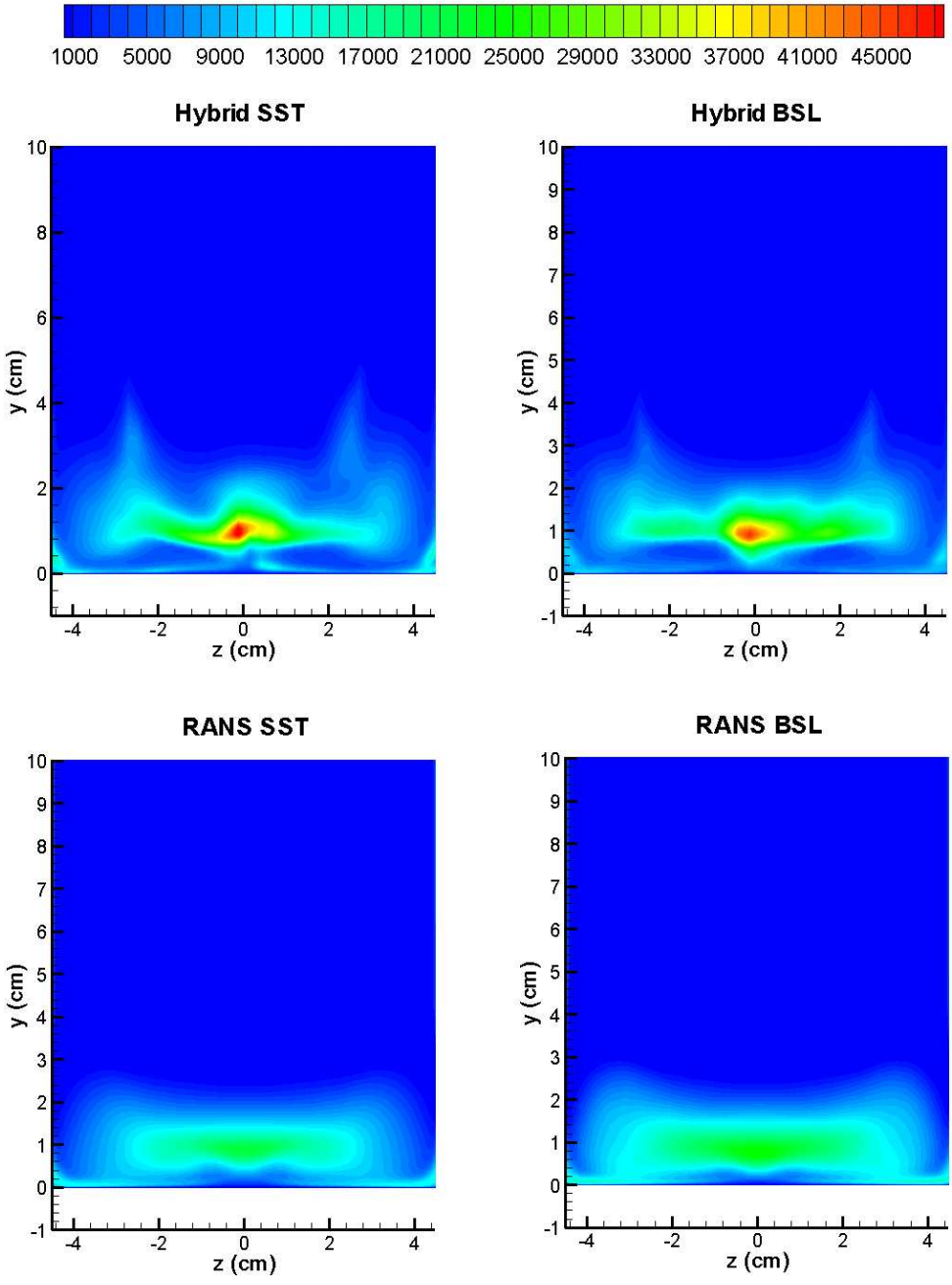

Figure 5.25: TKE contours at station 1, $k_{resolved}$ shown for the hybrid models (x = 18.2 cm)

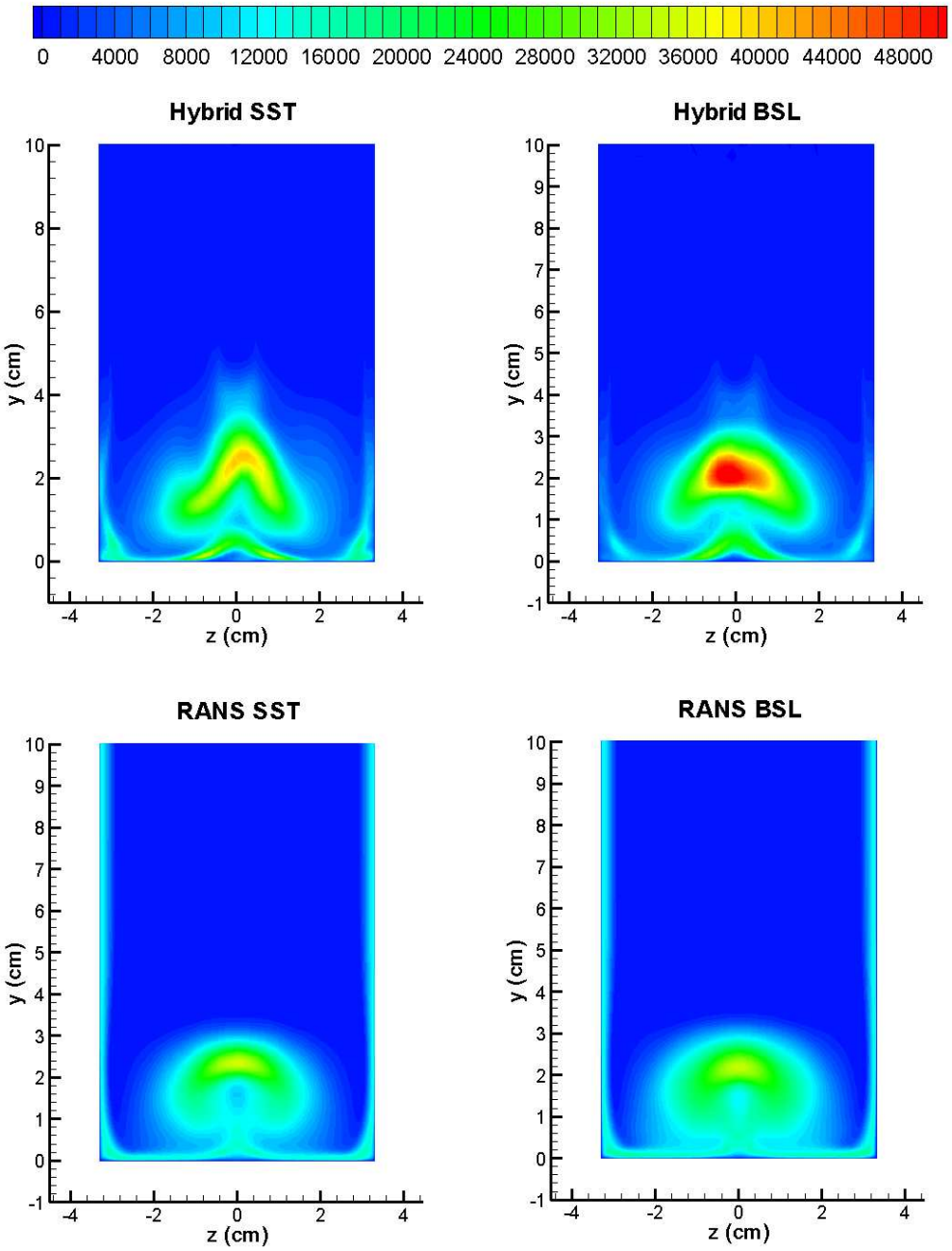

Figure 5.26: Resolved TKE contours at station 2, $k_{resolved}$ shown for the hybrid models (x = 26.0 cm)

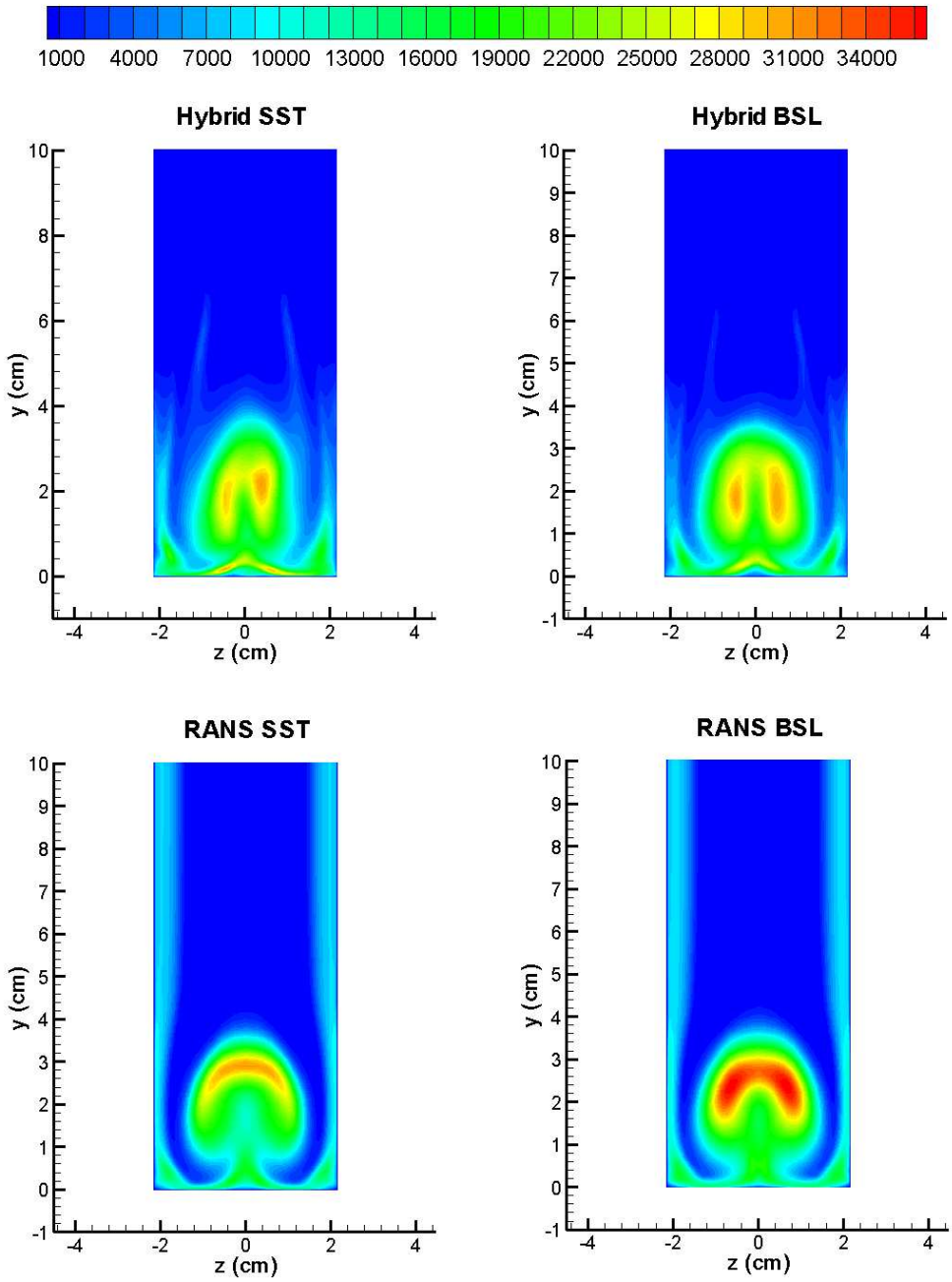

Figure 5.27: TKE contours at station 3, $k_{resolved}$ shown for the hybrid models (x = 34.0 cm)

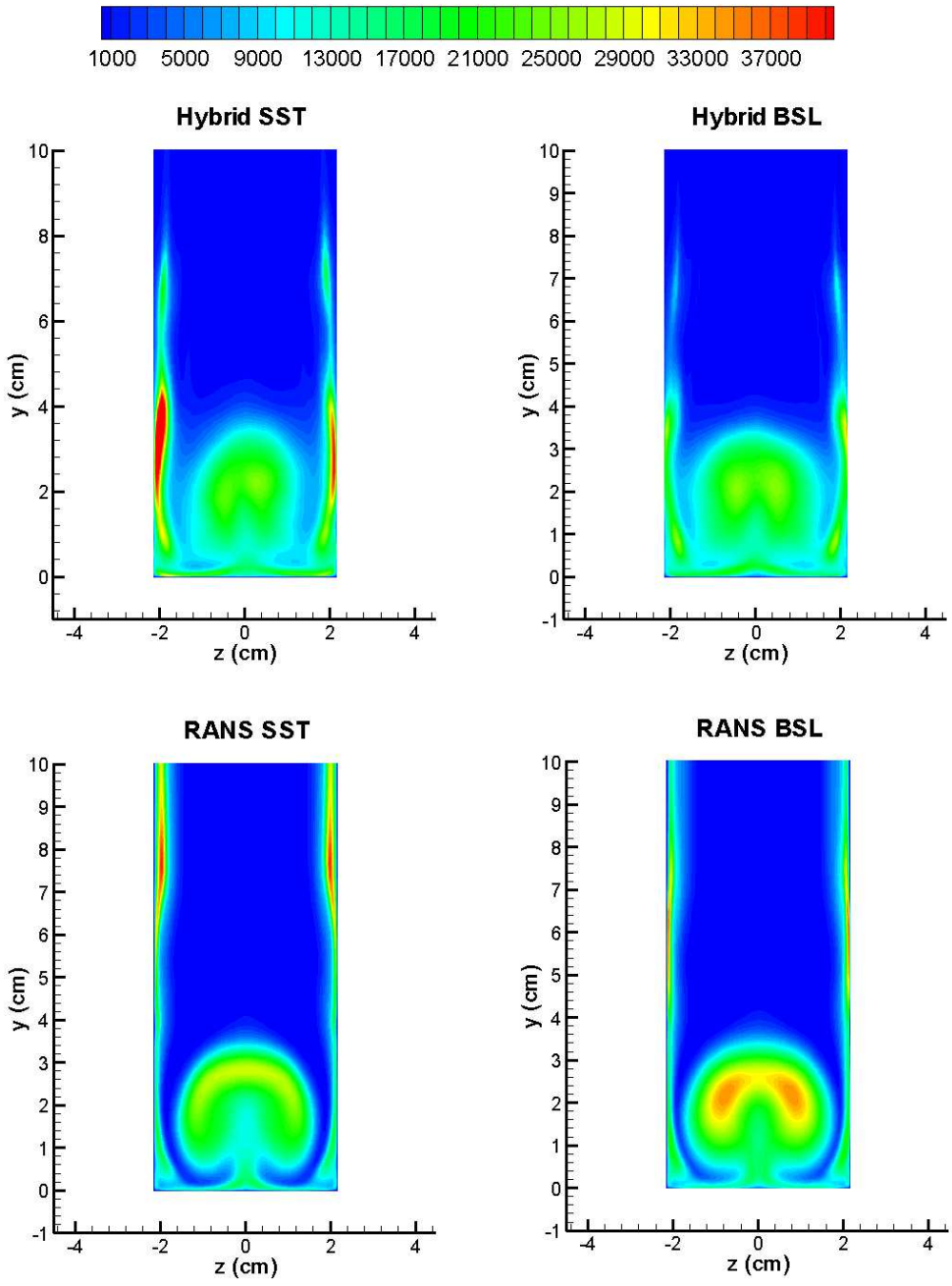

Figure 5.28: TKE contours at station 4, $k_{resolved}$ shown for the hybrid models (x = 38.3 cm)

Chapter 6

Conclusions

A hybrid LES/RANS model for simulating a crossing shock interaction has been presented in this study. This model incorporates fluid properties as well as wall distance into its computation of the transition from RANS to LES. This computation was compared with experimental data and RANS data, using both the Menter BSL and Menter SST for the RANS closure. The RANS model was used as a near-wall closure for a flow otherwise modeled by LES with Yoshizawa's subgrid kinetic energy model for closure.

The upstream boundary layer growth on the flat plate was well-predicted by the hybrid model, with the SST variation performing best. There was a significant improvement over the RANS calculations. The velocity profile for the hybrid case was particularly well-matched. The temperature profile was underpredicted for all the models tested, with the hybrid SST model performing the best still.

The hybrid method did not do as well in modeling the crossing shock interaction. Coarse-grid simulations of the entire interaction suggested that the hybrid model would be an improvement over RANS simulations. Unfortunately this trend did not hold with grid refinement. Both RANS models predicted nearly every experimental quantity provided more accurately than the hybrid LES/RANS models. The most glaring differences among the models were found in the predictions of wall heat transfer. The hybrid models greatly overpredicted heat transfer while the RANS models did an adequate job of predicting the centerline profile. No models accurately predicted the transverse wall heat transfer

One notable observation in this work is that LES is being used for nearly all of the flow downstream of the crossing shock. This could be a cause of the high heating loads for the hybrid SST model because the grid is not resolved enough close to the wall. As a

result, the near-wall turbulence intensity is over-predicted, which causes the over-prediction of heat transfer at the wall. This is also supported by the fact that the wall heat transfer prediction was reduced for the hybrid BSL case; this model generally yields higher eddy viscosity levels and thus turbulent fluctuations are reduced compared to its Menter SST counterpart. A possible solution to this problem is increasing the value of the transition parameter A so that the LES transition happens farther away from the wall.

Also, the more extreme 15° double fin case detailed in Ref. [1] needs to be tested. This simulation is more difficult because the shock wave is more intense, causing a larger separation in the flow in the converging solution. The resolution of the boundary layer on the fin walls is not adequate to capture the large-scale turbulent structures. The ramifications of this limitation are not as evident for the 10° fin case as was run in this study because the crossing shock does not impinge on the fins. It is expected that the 15° fin case [1] would be more sensitive to the boundary layer treatment.

Another possible avenue for future improvement of the method is to make the inflow boundary and the recycling/rescaling technique more random. As it stands now, the incoming turbulent boundary layer is extremely periodic. It is not clear if this has a significant negative impact on the solution, but a study into the effects of greater randomization could prove valuable.

Bibliography

[1] M. I. Kussoy and K. C. Horstman. Intersecting shock-wave / turbulent boundary layer interactions at Mach 8.3. NASA TM 103909, NASA Ames Research Center, February 1992.

[2] David S. Dolling. Fifty years of shock-wave/boundary-layer interaction research: What next? *AIAA Journal*, 39(8):1517–1531, August 2001.

[3] Charles G. Speziale. Turbulence modeling for time-dependent RANS and VLES: A review. *AIAA Journal*, 36(2):173–184, February 1998.

[4] David C. Wilcox. *Turbulence Modeling for CFD, Second Edition*, pages 381–392. DCW Industries, 1998.

[5] P.R. Spalart, W.-H. Jou, and S.R. Allmaras. Comments on the feasibility of LES for wings and on a hybrid RANS/LES approach. In *1st AFOSR Conference on DNS/LES*, Arlington, TX, August 1997.

[6] James R. Forsythe, Kyle D. Squires, Kenneth E. Wurtzler, and Philippe R. Spalart. Detached-eddy simulation of the F-15E at high alpha. *Journal of Aircraft*, 41(2):1629–1632, July 2004.

[7] D. Basu, A. Hamed, and K. Das. DES and hybrid RANS/LES models for unsteady separated turbulent flow predictions. In *43rd AIAA Aerospace Sciences Meeting & Exhibit*, number AIAA 2005-0503, Reno, Nevada, January 2005.

[8] Simon Dahlstrom and Lars Davidson. Hybrid RANS/LES employing interface condition with turbulent structure. In K. Hanjalic, Y. Nagao, and M. Tummers, editors, *Turbulence, Heat and Mass Transfer 4*. Begell House, Inc., New York, 2003.

[9] Lars Davidson and Simon Dahlstrom. Hybrid LES-RANS an approach to make LES applicable at high Reynolds number. In *ICHMT International Symposium on Advancements in Computational Heat Transfer*, Norway, April 2004.

[10] K. Hanjalic. Will RANS survive LES? A view of perspectives. *Journal of Fluids Engineering*, 127:831–839, September 2005.

[11] P. R. Spalart, S. Deck, M. L. Shur, K. D. Squires, M. Kh. Strelets, and A. Travin. A new version of detached-eddy simulation, resistant to ambiguous grid densities. *Theoretical Computational Fluid Dynamics*, 20:181–195, 2006.

[12] F. R. Menter. Two-equation eddy-viscosity turbulence models for engineering applications. *AIAA Journal*, 32(8):1598–1605, 1994.

[13] Paul Batten, Uriel Goldberg, and Sukumar Chakravathy. LNS – an approach towards embedded LES. AIAA Paper 2002-0427, 2002. AIAA Special Session on Alternative LES and RANS/LES.

[14] Frédéric Thivet, Doyle D. Knight, Alexander A. Zheltovodov, and Alexander I. Maksimov. Insights in turbulence modeling for crossing-shock-wave/boundary-layer interactions. *AIAA Journal*, 39(6):985–995, June 2001.

[15] Doyle D. Knight, C. C. Horstman, Brian Shapey, and Seymour Bogdonoff. Structure of supersonic turbulent flow past a sharp fin. *AIAA Journal*, 25(10):1331–1337, October 1987.

[16] Datta Gaitonde, J. S. Shang, and Miguel Visbal. Structure of a double-fin turbulent interaction at high speed. *AIAA Journal*, 33(2):193–200, February 1995.

[17] T. J. Garrison, G. S. Settles, N. Narayanswami, and D. D. Knight. Structure of crossing-shock-wave/turbulent-boundary-layer interactions. *AIAA Journal*, 31(12):2204–2211, December 1993.

[18] N. Narayanswami, C. C. Horstman, and D. D. Knight. Numerical simulation of crossing shock turbulent boundary layer interaction at Mach 8.3 - comparison of zero- and two-equation turbulence models. AIAA Paper 93-0779, 1993.

[19] P. A. Durbin. On the $k - \epsilon$ stagnation point anomaly. *International Journal of Heat and Fluid Flow*, 17(1):89–90, 1978.

[20] G. A. Gerolymos, E. Sauret, and I. Vallet. Oblique-shock-wave/boundary-layer interaction using near-wall Reynolds stress models. *AIAA Journal*, 42(6):1089–1100, June 2004.

[21] G. A. Gerolymos and I. Vallet. Wall-normal-free near-wall Reynolds-stress closure for three-dimensional compressible separated flows. *AIAA Journal*, 39(10):1833–1842, October 2001.

[22] John A. Boles and Jack R. Edwards. Hybrid large-eddy / Reynolds-averaged Navier-Stokes simulation of a Mach 8.3 crossing-shock interaction. In *36th AIAA Fluid Dynamics Conference*, number AIAA 2006-3039, San Francisco, California, June 2006.

[23] R.A. Baurle, J. Tam, J.R. Edwards, and H.A. Hassan. Hybrid LES/RANS approach for cavity flows: Blending, algorithm, and boundary treatment issues. *AIAA Journal*, 41(8):1463–1480, 2003.

[24] T. C. Fan, Xudong Xiao, J. R. Edwards, H. A. Hassan, and R. A. Baurle. Hybrid large-eddy/Reynolds-averaged Navier-Stokes simulations of shock-separated flows. *Journal of Spacecraft and Rockets*, 41(6):897–906, 2004.

[25] Doyle D. Knight and Gerard Degrez. Shock wave boundary layer interactions in high Mach number flows. a critical survey of current CFD prediction capabilities. Advisory Report 319, AGARD, December 1998.

[26] Akira Yoshizawa and Kiyosi Horiuti. A statistically-derived subgrid-scale kinetic energy model for the large-eddy simulation of turbulent flows. *Journal of the Physical Society of Japan*, 54(8):2834–2839, 1985.

[27] Charles Hirsch. *Numerical Computation of Internal and External Flows*, volume 1: Computational Methods for Invsicid and Viscous Flows, pages 49–51. John Wiley and Sons, 1988.

[28] F. R. Menter. Influence of freestream values on k-ω tubulence model predictions. *AIAA Journal*, 30(6):1651–1659, 1992.

[29] D. A. Johnson and L. S. King. Mathematically simple turbulence closure model for attached and separated turbulent boundary layers. *AIAA Journal*, 23(11):1684–1692, 1985.

[30] P. Bradshaw, D. H. Ferriss, and N. P. Atwell. Calculation of boundary-layer development using the turbulent energy equation. *Journal of Fluid Mechanics*, 28(3):593–616, 1967.

[31] J.R. Edwards. A low-diffusion flux-splitting scheme for Navier-Stokes calculations. *Computers and Fluids*, 26(6):635–659, 1997.

[32] A. Suresh and H.T. Huynh. Numerical experiments on a new class of nonoscillatory schemes. paper 92-0421, AIAA Journal, 1992.

[33] V. Venkatakrishnan. On the accuracy of limiters and convergence to steady-state solutions. AIAA Paper 93-0880, 1993.

[34] Thomas C. Fan. Hybrid Reynolds-averaged / large-eddy simulations of ramped-cavity and compression ramp flow-fields. Master's thesis, North Carolina State University, July 2002.

[35] Keith McDaniels. Three dimensional simulation of a time-dependent scramjet isolator/combustor flowfields implemented on parallel architectures. Master's thesis, North Carolina State University, December 2000.

[36] Jason B. Star. *Numerical Simulation of Scramjet Combustion in a Shock Tunnel*. PhD thesis, North Carolina State University, December 2005.

[37] Jack R. Edwards, Xudong Xiao, and Hassan Hassan. Hybrid large-eddy / Reynolds-averaged Navier-Stokes simulation of Mach 8.3 flow over a flat plate. AIAA Paper 2005-0882, 2005.

Appendices

Appendix A

Model Constants

σ_{k1}	=	0.5	σ_{k2}	=	1.0
$\sigma_{\omega 1}$	=	0.5	$\sigma_{\omega 2}$	=	0.856
β_1	=	0.0750	β_2	=	0.0828
γ_1	=	0.5532	γ_2	=	0.4404
β^*	=	0.09	C_μ	=	0.09
C_s	=	0.04641	C_d	=	1.0

For the constants used in the Menter RANS regime of the flow, the combined constants (σ_k,σ_ω,β and γ) can be found as follows (with ϕ being a generic constant):

$$\phi = F_1\phi_1 + (1 - F_1)\,\phi_2 \tag{A.1}$$

The constants detailed above are assuming Menter RANS BSL. For the SST modification, $\sigma_{k1} = 0.81$.

Appendix B

Blending Function Proof

This appendix will prove the claim that $d^+ = A^2$ at the RANS/LES transition point when assuming log-law relations. The blending function, Γ is defined as:

$$\Gamma = \frac{1}{2}\left\{1 - \tanh\left[5\left(\frac{\kappa}{\sqrt{C_\mu}}\eta^2 - 1\right)\right]\right\} \tag{B.1}$$

At the RANS/LES transition point $\Gamma = 0.5$ thus:

$$\frac{1}{2}\left\{1 - \tanh\left[5\left(\frac{\kappa}{\sqrt{C_\mu}}\eta^2 - 1\right)\right]\right\} = \frac{1}{2} \tag{B.2}$$

$$\tanh\left[5\left(\frac{\kappa}{\sqrt{C_\mu}}\eta^2 - 1\right)\right] = 0 \tag{B.3}$$

$$\frac{\kappa}{\sqrt{C_\mu}}\eta^2 - 1 = 0 \tag{B.4}$$

with

$$\eta = \frac{d}{A\gamma} \tag{B.5}$$

$$\gamma = \sqrt{\frac{\nu}{C_\mu \omega}} \tag{B.6}$$

$$d^+ = \frac{du_\tau}{\nu} \tag{B.7}$$

then Equation B.4 yields:

$$A^2 = \frac{d^2}{\gamma^2}\frac{\kappa}{\sqrt{C_\mu}} \tag{B.8}$$

$$= \frac{d^2}{\left(\frac{\nu}{C_\mu \omega}\right)}\frac{\kappa}{\sqrt{C_\mu}} \tag{B.9}$$

The log-law assumption gives:

$$\omega = \frac{u_\tau}{\sqrt{\beta^*}\kappa d} \tag{B.10}$$

which when applied to Equation B.9 gives:

$$A^2 = \frac{d^2}{\left(\frac{\nu\sqrt{\beta^*}\kappa d}{C_\mu u_\tau}\right)}\frac{\kappa}{\sqrt{C_\mu}} \tag{B.11}$$

$$= \frac{d u_\tau \sqrt{C_\mu}}{\nu\sqrt{\beta^*}} \tag{B.12}$$

using Equation B.7:

$$A^2 = \frac{\frac{d^+\nu}{u_\tau} u_\tau \sqrt{C_\mu}}{\nu\sqrt{\beta^*}} \tag{B.13}$$

$$= \frac{d^+\sqrt{C_\mu}}{\sqrt{\beta^*}} \tag{B.14}$$

Since $C_\mu = \beta^* = 0.09$, $A^2 = d^+$.